Thesis for Master's Degree

A Spectral Flux-Shaping Finite-Volume Method with Zero Pass-Band Dissipation: A Low-Dissipation Conservative Scheme Based on Upwind Flux Splitting

Chanho Park

School of Mechanical Engineering

Gwangju Institute of Science and Technology

2026

A Spectral Flux-Shaping Finite-Volume Method with Zero Pass-Band Dissipation: A Low-Dissipation Conservative Scheme Based on Upwind Flux Splitting

항공음향 해석을 위한 스펙트럼 쉐이핑 기반 DRP 유한체적법 연구

A Spectral Flux-Shaping Finite-Volume Method with Zero Pass-Band Dissipation: A Low-Dissipation Conservative Scheme Based on Upwind Flux Splitting

Advisor: Seongim Choi

by

Chanho Park

School of Mechanical Engineering

Gwangju Institute of Science and Technology

A thesis submitted to the faculty of the Gwangju Institute of Science and Technology in partial fulfillment of the requirements for the degree of Master of Science in the School of Mechanical Engineering

Gwangju, Republic of Korea

December 26, 2025

Approved by

Professor Seongim Choi

Committee Chair

A Spectral Flux-Shaping Finite-Volume Method with Zero Pass-Band Dissipation: A Low-Dissipation Conservative Scheme Based on Upwind Flux Splitting

Chanho Park

Accepted in partial fulfillment of the requirements for

the degree of Master of Science

2025 12, 26

Committee Chair _____
Seongim Choi

Committee Member _____
Ray-Sing Lin

Committee Member _____
Taeseong Kim

To those who saw the brilliance in me, even when I could not.

MS/ME 20234025 Chanho Park. A Spectral Flux-Shaping Finite-Volume Method with Zero Pass-Band Dissipation: A Low-Dissipation Conservative Scheme Based on Upwind Flux Splitting. School of Mechanical Engineering. 2026. 61p. Advisor: Prof. Seongim Choi.

Abstract

High-order numerical schemes for computational aeroacoustics (CAA) must exhibit extremely low dispersion and dissipation to accurately propagate acoustic waves. However, such schemes often lack the robustness required to handle flows with shocks, while classical shock-capturing schemes are typically too dissipative for high-fidelity acoustics. This thesis introduces a Spectral Flux-Shaping Finite-Volume Method (SFS-FVM) that reconciles these competing requirements through a novel flux-shaping technique based on compact Padé operators. The method is applied to standard upwind flux-splitting schemes, such as Roe and AUSM+up.

By separating the numerical flux into distinct transport and diffusive paths, we apply a compact operator to correct dispersion errors on the transport path and a separate spectral bump operator to precisely control dissipation on the diffusive path. This approach enables a Zero Pass-Band Dissipation (ZPD) design that completely eliminates numerical damping for well-resolved waves in smooth flow regions. To ensure nonlinear stability, a sensor-based gating mechanism smoothly reverts the scheme to its baseline shock-capturing formulation near discontinuities. Unlike central schemes that rely on tunable artificial viscosity, this strategy recovers the intrinsic, physics-based stability of the approximate Riemann solver at shocks.

We validate the method on a suite of canonical test cases, ranging from fundamental wave advection to complex shock-entropy interactions and multi-dimensional pulse propagation in a mean flow. The results demonstrate that SFS-FVM significantly reduces dispersion and dissipation errors compared to baseline solvers, achieving an

error reduction of approximately 50% in shock-turbulence interaction problems, while maintaining non-oscillatory robustness for strong discontinuities. The proposed framework successfully unifies high-fidelity wave propagation with shock-capturing reliability within a single, conservative finite-volume context.

MS/ME 박찬호. 항공음향 해석을 위한 스펙트럼 쉐이핑 기반 DRP 유한체적법 연구.
20234025 기계공학부. 2026. 61p. 지도교수: 최성임.

국 문 요 약

전산공력음향학(CAA)을 위한 고차 수치 기법은 음향 파동을 정확하게 전파하기 위해 매우 낮은 분산 및 소산 오차를 보여야 합니다. 그러나 이러한 기법들은 충격파가 존재하는 유동을 다루는 데 필요한 강건성이 부족한 경우가 많으며, 반면 고전적인 충격파 포착 기법들은 고정밀 음향학을 위해서는 소산이 너무 심한 경향이 있습니다.

본 논문은 이러한 상충되는 요구 사항을 해결하기 위해 콤팩트 파데(Padé) 연산자에 기반한 새로운 플럭스 형성 기법인 스펙트럼 플럭스 형성 유한 체적법(SFS-FVM)을 제안합니다. 이 방법은 Roe 및 AUSM+up과 같은 표준 상류 플럭스 분할 기법에 적용됩니다. 수치 플럭스를 별도의 이송(transport) 및 확산(diffusive) 경로로 분리함으로써, 이송 경로에는 분산 오차를 보정하기 위해 콤팩트 연산자를 적용하고, 확산 경로에는 소산을 정밀하게 제어하기 위해 별도의 스펙트럼 범프 연산자를 적용합니다. 이러한 접근 방식은 매끄러운 유동 영역에서 잘 분해된 파동에 대한 수치적 감쇠를 완전히 제거하는 영-통과대역 소산(Zero Pass-Band Dissipation, ZPD) 설계를 가능하게 합니다.

비선형 안정성을 보장하기 위해, 센서 기반의 게이팅 메커니즘이 불연속면 근처에서 기법을 기존의 충격파 포착 형태로 부드럽게 전환합니다. 조정 가능한 인공 점성에 의존하는 중앙 차분 기법들과 달리, 이 전략은 충격파에서 근사 리만 솔버의 고유한 물리 기반 안정성을 회복합니다.

본 연구에서는 기본적인 파동 이송부터 복잡한 충격파-엔트로피 상호작용, 그리고 평균 유동 내 다차원 펄스 전파(multi-dimensional pulse propagation in a mean flow)에 이르는 일련의 표준 테스트 케이스를 통해 이 방법을 검증했습니다. 결과적으로 SFS-FVM은 기본 솔버 대비 분산 및 소산 오차를 획기적으로 줄였으며, 특히 충격파-난류 상호작용 문제에서 약 50%의 오차 감소를 달성함과 동시에 강한 불연속면에서 비진동 강건성을 유지함을 확인했습니다. 제안된 프레임워크는 단일 보존형 유한 체적 맥락

내에서 고정밀 파동 전파와 충격파 포착 신뢰성을 성공적으로 통합합니다.

Contents

List of Tables

List of Figures

Chapter 1

Introduction

1.1 Research Background

Accurate prediction of flow-generated noise requires numerical schemes with extremely low dispersion and dissipation errors. In computational aeroacoustics (CAA), where acoustic perturbations are often orders of magnitude smaller than the convective flow, any numerical phase error or excessive damping can corrupt the propagating sound waves [1].

Early works by Tam and others emphasized that resolving acoustic waves with minimal numerical attenuation or dispersion is essential for reliable simulations of noise propagation [2, 3, 4]. Tam's foundational dispersion-relation-preserving (DRP) schemes [3] were among the first to specifically target these requirements, optimizing finite-difference stencils so that numerical phase speeds closely match the physical dispersion relation over a wide range of wavenumbers. Subsequent reviews and benchmark studies have reiterated the stringent accuracy demands of CAA [5, 6], as do more recent best-practice assessments and overviews focused on low-dissipation/low-dispersion simulation of aeroacoustic sources [7, 8].

1.2 Literature Review

1.2.1 High-Order Numerical Methods

Building on the need for high fidelity, numerous high-order numerical methods have been developed to minimize dispersion and dissipation errors in acoustics. Tam and Webb's DRP finite-difference scheme [3] demonstrated that carefully optimized 7-point central differencing could substantially improve the resolution of short waves (down to about 6–8 points per wavelength) compared to standard schemes. Other researchers pursued alternative routes to high fidelity. Lele's compact finite differences [9] introduced

implicit Padé schemes achieving spectral-like resolution on smaller stencils, at the cost of solving tridiagonal systems. Ashcroft and Zhang [10] proposed optimized prefactored compact (OPC) schemes, further reducing dispersive error with a two-step explicit formulation. Bogey and Bailly [11] designed a family of explicit high-order schemes with low dispersion and low dissipation, combining optimized finite differences with mild filtering to control numerical oscillations. In the temporal domain, special low-dispersion Runge–Kutta time integrators have been formulated [12, 13] to pair with these spatial discretizations, and recent low-dissipation/low-dispersion time marching specifically tailored for aeroacoustics has been proposed [14]. High-order methods have also been extended to complex geometries. For example, Cheong and Lee [15] developed DRP schemes on curvilinear mapped grids, and Chang's space–time Conservation Element/Solution Element (CE/SE) method [16] provided an alternative high-resolution framework applicable to multidimensional flows. More recently, DRP-like ideas have been embedded in energy-stable flux-reconstruction and generalized summation-by-parts (SBP) frameworks to deliver near-spectral transport while retaining stability guarantees [17, 18]. Overall, a variety of high-fidelity approaches—including central and compact finite differences, explicit filtering techniques, and tailored finite-volume schemes—have been brought to bear on aeroacoustic problems.

1.2.2 The Accuracy-Stability Dichotomy

Despite these developments, significant challenges remain in reconciling dispersion accuracy with nonlinear robustness. Many DRP methods that excel for smooth acoustics encounter difficulties in the presence of shocks or strong flow gradients. Classical DRP-type finite differences [3, 4] and compact schemes [9] are non-dissipative and non-conservative, which means that even very small unresolved flow scales or slight discontinuities can trigger non-physical oscillations (Gibbs phenomena) unless supplemental damping is introduced.

Indeed, it is well documented that purely central high-order schemes require some form of numerical dissipation or filtering to handle steep gradients. Researchers have proposed adding explicit filtering or artificial viscosity to stabilize such schemes. These approaches include demonstrating that high-order artificial viscosity can enable stable shock resolution, investigating how various damping terms affect accuracy, and

introducing conservative smoothing on adaptive grids to control spurious oscillations [19, 20, 21, 22]. While these fixes suppress non-linear instabilities, they inevitably degrade spectral accuracy if over-applied.

On the other hand, shock-capturing upwind schemes—rooted in Godunov's finite-volume paradigm [23]—prioritize stability at discontinuities but typically at the expense of higher dissipation and phase error on smooth waves. The original total-variation-diminishing (TVD) schemes of Harten [24] and the Essentially Non-Oscillatory (ENO) schemes by Shu and Osher [25] were pivotal in providing nonlinear stability for capturing shocks without spurious ringing, and later WENO methods [26, 27] further improved accuracy and smoothness in shock-transition regions. However, even a fifth-order WENO scheme can substantially damp and disperse high-frequency acoustic content. In a comprehensive benchmark study, Johnsen et al. [28] showed that high-order WENO and TVD schemes dissipate small-scale turbulent structures and acoustic fluctuations more severely than central schemes of comparable order, underscoring the trade-off between shock-resolving robustness and wave-preserving fidelity.

1.2.3 Hybrid and Adaptive Strategies

To mitigate such issues, researchers have explored hybrid and improved algorithms. Yee et al. [29] (see also [30]) developed high-order filter schemes that apply targeted filtering (characteristic-based or localized) to damp only the high-wavenumber oscillations, preserving resolved scales. Adaptive nonlinear dissipation control has been another strategy: for instance, [31, 32, 33] formulated variants with adaptive dissipation, reducing numerical damping in smooth regions while still capturing discontinuities. Kawai and Lele's localized artificial diffusivity (LAD) method [34] represents a successful approach in which a sensor adds minimal viscosity at shocks and nowhere else, enabling essentially central schemes to compute shock–turbulence interactions with low background dissipation. Pirozzoli [35] provided a spectral analysis of such nonlinear schemes, showing how one can in principle tune dispersion and dissipation errors independently; nevertheless, some dissipation is necessary to maintain stability for under-resolved waves. Bogey et al. [36] pursued a different route by using explicit spatial filtering on central schemes to capture shock cells in jets—an approach that acted as an implicit LES and minimized acoustic contamination.

1.3 Research Motivation and Contribution

Despite these advances, the fundamental compromise remains: methods designed for smooth-region accuracy tend to lack robustness at discontinuities, whereas schemes built for shock stability tend to damp fine-scale acoustics. This long-standing dichotomy motivates the present work and has driven ongoing research into schemes that can *simultaneously* achieve low dispersion and controllable dissipation [37]. For example, recent DRP-oriented formulations blend low-dispersion transport with locally adaptive dissipation to respond to evolving flow features [38, 32], thereby preserving wave fidelity in smooth regions while introducing just enough damping near shocks and under-resolved gradients.

In this thesis, we address the above challenge by developing a Spectral Flux-Shaping Finite-Volume Method (SFS-FVM) that embeds high-fidelity wave propagation capabilities within a conservative, shock-capturing framework. Finite-volume schemes are attractive for compressible flow acoustics because of their conservative formulation and flexibility on complex meshes [39], but to date, many high-order FVMs have not explicitly targeted dispersion error reduction. Nance et al. and Gutierrez Pimenta et al. presented early attempts to marry DRP principles with a finite-volume discretization, formulating low-dispersion FVM versions [40, 41]. They demonstrated that the finite-volume variants yield substantially better results in nonlinear cases (e.g., shock–acoustic interactions) than the original finite-difference schemes, thanks to the inherent conservation and the use of Riemann solvers at cell interfaces.

Our approach builds on this idea and significantly extends it by introducing a novel flux decomposition strategy. Rather than depending on ad-hoc, user-calibrated damping coefficients to stabilize shocks, we separate the numerical flux into distinct transport and diffusive paths. This allows us to apply compact Padé filters to cancel dispersion errors on the transport path while enforcing a Zero Pass-Band Dissipation (ZPD) condition on the diffusive path. For shock stability, we employ a characteristic-wise flux split (e.g., Roe or AUSM+up [42, 43]) combined with a sensor-based gating mechanism. This mechanism smoothly reverts the scheme to its baseline shock-capturing formulation only in the immediate vicinity of discontinuities. The result is a method that preserves phase accuracy and low amplitude decay for acoustic waves, yet recovers the intrinsic physics-based stability of the approximate Riemann solver at shocks.

We validate this SFS-FVM on a suite of canonical test cases ranging from linear acoustics to complex nonlinear flows. The former demonstrate that the scheme's dispersion and dissipation errors are significantly lower than those of conventional high-order upwind methods, and close to the ideal linear dispersion relation up to high wavenumbers. The latter—including shock-tube problems, shock–entropy interaction, and multi-dimensional pulse propagation in a mean flow—confirm that the method captures discontinuities and fine-scale eddies without spurious oscillations, while improving the resolution of fine-scale features compared to standard shock-capturing schemes.

1.4 Thesis Outline

The remainder of this thesis is organized as follows. Chapter 2 describes the numerical formulation of the SFS-FVM scheme, detailing the decomposition of flux into transport and diffusive paths, the spectral shaping via compact operators, and the sensor-based gating mechanism for shock robustness. Chapter 3 presents the comprehensive numerical results, quantifying the dispersion and dissipation characteristics in comparison to baseline schemes and examining the method's performance on nonlinear problems representative of shock–turbulence interaction and CAA benchmarks. Finally, Chapter 4 offers conclusions and an outlook for further improvements and applications of the proposed SFS-FVM approach.

Chapter 2

Methodology

In this section, we develop our flux-shaping methodology in a series of logical steps. We begin by reviewing the finite-volume framework. We then introduce our core strategy of separating the numerical flux into distinct transport and diffusive paths. Following this, we establish the design requirements for the spectral 'shapers' that will be applied to each path and detail their construction using compact Padé operators. Finally, we describe the sensor-based gating mechanism for shock robustness and present the formal guarantees of the completed scheme.

2.1 Finite-volume update and reconstruction symbols

All numerical schemes in this work are built upon a conservative finite-volume (FV) framework. On a uniform grid, the semi-discrete FV update for the vector of conserved quantities $\bar{\mathbf{U}}_i$ in cell i is given by

$$\frac{\mathrm{d}\bar{\mathbf{U}}_i}{\mathrm{d}t} = -\frac{\widehat{\mathbf{F}}_{i+\frac{1}{2}} - \widehat{\mathbf{F}}_{i-\frac{1}{2}}}{h}, \qquad \mathbf{U} = [\rho, \rho u, E]^\top, \quad p = (\gamma - 1)\Big(E - \tfrac{1}{2}\rho u^2\Big)\,. \tag{2.1}$$

This equation expresses the fundamental principle of conservation: the rate of change of a quantity within a cell (e.g., density ρ, momentum ρu, or total energy E) is equal to the net flux of that quantity across its boundaries. Here, $\widehat{\mathbf{F}}_{i\pm\frac{1}{2}}$ represents the numerical flux at the left and right cell faces, and h is the cell width. A key challenge in FV methods is that while the state $\bar{\mathbf{U}}_i$ is known as a cell-average, the flux $\widehat{\mathbf{F}}$ must be evaluated at the cell interfaces. This requires *reconstructing* the solution from cell centers to the faces. The accuracy of this reconstruction step is paramount for high-fidelity simulations.

We can precisely quantify the behavior of a given reconstruction scheme for a planar wave using its reconstruction symbol, or transport factor, $\alpha(\theta = kh)$ [44]. This function, derived from Fourier analysis in the modified-wavenumber view, reveals how

well the discrete scheme represents a wave with a normalized wavenumber θ. In an ideal, error-free scheme, the symbol would be exactly $\alpha(\theta) = \theta$. For common schemes, it is an approximation (see Appendix A for details):

$$\alpha_{\text{CD2}} = \sin\theta, \qquad \alpha_{\text{CD4}} = \alpha_{\text{MUSCL3}} = \frac{8\sin\theta - \sin 2\theta}{6}, \qquad \alpha_{\text{MUSCL2(BW)}} = (2-\cos\theta)\sin\theta. \tag{2.2}$$

To better understand the deficiencies of these schemes, we can analyze their small-angle expansions, which act as a magnifying glass on the errors for well-resolved, long-wavelength phenomena. An expansion of the form $\alpha(\theta) = \theta + c_3\theta^3 + c_5\theta^5 + \cdots$ exposes the leading-order dispersion errors—the terms that cause numerical waves to propagate at the wrong speed:

$$\begin{aligned} \textbf{CD2:} \quad & \alpha(\theta) = \theta - \tfrac{1}{6}\theta^3 + \tfrac{1}{120}\theta^5 + \mathcal{O}(\theta^7), \\ \textbf{CD4/MUSCL3:} \quad & \alpha(\theta) = \theta - \tfrac{1}{30}\theta^5 + \mathcal{O}(\theta^7), \\ \textbf{MUSCL2:} \quad & \alpha(\theta) = \theta + \tfrac{1}{3}\theta^3 - \tfrac{7}{60}\theta^5 + \mathcal{O}(\theta^7). \end{aligned} \tag{2.3}$$

The central idea of our proposed method is to design a "transport shaper" that specifically targets and cancels these error terms. The coefficients of the error, (c_3, c_5), serve as the precise "fingerprints" of the dispersion that must be eliminated. These coefficients are therefore used to impose the moment conditions in the Padé transport fit, as detailed in Section 2.3.

2.2 Flux Path Separation and Shaper Design Requirements

The central strategy of our method is to isolate the physical mechanisms within the numerical flux that are responsible for dispersion and dissipation. By separating the flux into distinct "paths," we can correct the errors on each path independently. Following the general principle of upwind flux splitting, we employ each solver's native decomposition and apply DRP shaping *per path*. The nondissipative central component, which governs wave propagation, carries the dispersion error, while the upwind part, which ensures stability, carries the numerical damping. This separation underpins modern shock-capturing and localized-diffusion/filter ideas; we therefore shape the

transport path for low dispersion and the diffusive path for controlled high-θ damping.

Roe. For the Roe solver, this separation is explicit. The numerical flux is the sum of a non-dissipative central average (the transport path) and an upwind dissipation term (the diffusive path):

$$\widehat{\mathbf{F}} = \underbrace{\tfrac{1}{2}\big(\mathbf{F}(\mathbf{U}^L) + \mathbf{F}(\mathbf{U}^R)\big)}_{\mathbf{F}^{\mathrm{c}}\text{: transport}} - \underbrace{\tfrac{1}{2}\sum_k |\lambda_k|\ \beta_k\, \mathbf{r}_k}_{\mathbf{D}\text{: diffusion}}, \tag{2.4}$$

where $\mathbf{F}^{\mathrm{c}}$ is the dispersion-bearing central flux and $\mathbf{D}$ is purely dissipative. The terms λ_k, $\mathbf{r}_k$, and β_k denote, respectively, the characteristic speeds, right eigenvectors, and wave strengths of the Roe linearization, which physically represent the wave structure of the flow.

AUSM +up. Similarly, the AUSM+up scheme possesses a natural separation. We recast its standard decomposition into a centralized form (see Appendix A.3.1) to make the two paths clear:

$$\widehat{\mathbf{F}} \;=\; \underbrace{\widehat{\mathbf{F}}^{\mathrm{adv}} + \widehat{\mathbf{F}}^{\mathrm{press}}}_{\text{central/dispersion-bearing}} \;+\; \underbrace{\widehat{\mathbf{F}}^{\mathrm{UP}}}_{\text{purely dissipative}} \quad . \tag{2.5}$$

Here, the advective and pressure fluxes form a purely central, dispersion-bearing transport path, governed by the low-Mach gate $\phi = 1 - \min(1, \overline{M^2})$. The stability and damping are entirely contained within the purely dissipative upwind flux, $\widehat{\mathbf{F}}^{\mathrm{UP}}$.

This strategy of splitting the flux at the cell face offers several crucial advantages. First, it enables independent control of dispersion and dissipation; we can correct phase errors in the transport path without altering the damping characteristics of the diffusive path, and vice versa. Second, because the shaping is applied to the flux before the final divergence is computed, the method preserves conservation and freestream properties automatically. Finally, this approach aligns with the solver's physics, respecting the native structure of each scheme (e.g., Roe's characteristic waves or AUSM's Mach-gated upwinding) to achieve high fidelity without compromising the solver's inherent

robustness.

To realize this control, we introduce two spectral "shapers" applied to the respective paths: a transport shaper, $g_A(\theta)$, designed to cancel dispersion error, and a diffusion shaper, $g_D(\theta)$, to control numerical damping. The successful design of these shapers hinges on satisfying a set of rigorous requirements that ensure accuracy, stability, and physical consistency. These rules, consolidated below, guide the construction of the bounded Padé transport shaper and the monotone diffusion bump used in our design.

Requirement	Explanation
R1. Locality & Compactness	**Efficiency and simplicity.** Relies solely on compact stencils (neighboring points) to facilitate boundary treatment and avoid global operations like FFTs.
R2. Conservation & Freestream	**Physical consistency.** Must strictly preserve conservation laws (mass/energy) and leave uniform flow states (freestreams) invariant.
R3. Transport Accuracy	**Dispersion cancellation.** Must actively correct phase errors in the base scheme, yielding near-perfect propagation for acoustic waves within the resolved "pass band."
R4. Bounded Gain	**Noise control.** The shaping gain is strictly bounded ($\|g\| \leq g_{\max}$) to prevent the amplification of numerical noise into instabilities.
R5. Nonnegative Diffusion	**Stability preservation.** The shaper must never inject energy. It scales the numerical damping magnitude but preserves its sign to guarantee stability.
R6. Zero Pass-Band Dissipation (ZPD)	**Lossless propagation.** (AUSM+up) Numerical damping is completely deactivated for resolved waves in smooth regions, preventing artificial signal attenuation.

Requirement	Explanation
R7. Shock Robustness & Gating	**Safety mechanism.** Shaping is disabled ($g = 1$) at discontinuities, reverting to the robust baseline solver; shaping acts only as a modifier in smooth zones.

2.3 Transport shaper: bounded Padé and its compact realization

To counteract the dispersion error of the base scheme, we design a corrective "shaper," or gain function, denoted by $g_A(\theta)$. This shaper acts like a custom-tuned filter applied to the transport path. We choose a powerful and flexible form for this function known as a rational Padé(4,4) function [45]:

$$g_A(\theta) = \frac{1 + c_2\theta^2 + c_4\theta^4}{1 + d_2\theta^2 + d_4\theta^4}, \qquad g_A(0) = 1, \quad g_A(\theta) \le g_{A,\max}. \tag{2.6}$$

This blueprint for our filter is governed by the coefficients (c_2, c_4, d_2, d_4), which are the "tuning knobs" we will adjust to achieve our desired accuracy. The constraints ensure that the shaper respects fundamental physics: it does nothing to a uniform flow ($g_A(0) = 1$, satisfying R2) and is forbidden from amplifying noise ($g_A(\theta) \le g_{A,\max}$, satisfying R4).

It is worth noting that our use of the Padé form differs from the classical compact finite-difference schemes of Lele [9]. In Lele's formulation, the Padé coefficients define a discrete spatial derivative operator. Here, they instead define a *spectral gain function* applied to the numerical fluxes: the Padé form serves as a flexible parametric filter template, not as a spatial discretization stencil.

The Padé gain is defined in Fourier space (as a function of θ), but it must be applied efficiently on our physical grid. We achieve this using a compact operator, a computational stencil that translates the frequency-space blueprint into a practical algorithm. Any real-even target function $g(\theta)$ can be implemented exactly using the

following pentadiagonal compact relation:

$$Y_j + a_1(Y_{j-1} + Y_{j+1}) + a_2(Y_{j-2} + Y_{j+2}) = b_0 X_j + b_1(X_{j-1} + X_{j+1}) + b_2(X_{j-2} + X_{j+2}). \quad (2.7)$$

Here, $\{X_j\}$ represents the original, uncorrected flux values at the cell faces, and $\{Y_j\}$ represents the new, corrected flux values. This operator is "compact" because it only requires information from immediate neighbors, making it highly efficient ($O(N)$ complexity) and easy to implement near boundaries (satisfying R1). Its key advantage is that the discrete Fourier response is exact: $\widehat{Y}(\theta) = g(\theta)\widehat{X}(\theta)$. To ensure the system is stable and yields a unique solution, we enforce the strict diagonal dominance condition during the fitting process:

$$1 - 2(|a_1| + |a_2|) \; > \; 0. \quad (2.8)$$

The choice of a Padé gain realized by a compact operator is motivated by several powerful advantages that directly satisfy our primary design requirements (R1–R4):

(a) *Exact modal control with a sparse stencil.* The rational form yields the exact frequency response without long explicit filters.

(b) *Low-angle "maximum flatness".* With the reconstruction factor $\alpha(\theta) = \theta + c_3\theta^3 + c_5\theta^5 + \cdots$, we enforce $g_A(\theta)\alpha(\theta) = \theta + \mathcal{O}(\theta^5)$, cancelling the cubic transport error and optionally reducing the quintic term on the pass band.

(c) *Bounded gain and good conditioning.* The denominator in (2.6) is kept positive (no poles), and we constrain $g_A \leq g_{A,\max}$ (we use $g_{A,\max} = 2$) to avoid amplification and keep the compact system well-conditioned.

(d) *Boundary-friendly, local, conservative.* The compact operator acts on *flux paths* at faces (not on states), uses the same halo as the flux, requires no global FFT/DCT, and preserves conservation/freestream automatically.

To operate the machine, we need a direct link between the blueprint's Padé coefficients (c_k, d_k) and the operator's stencil coefficients (a_k, b_k). This is achieved through an exact mathematical mapping. By equating the Padé form with the cosine ratio

representation of the compact stencil,

$$g_A(\theta) = \frac{b_0 + 2b_1 \cos\theta + 2b_2 \cos 2\theta}{1 + 2a_1 \cos\theta + 2a_2 \cos 2\theta}, \tag{2.9}$$

we derive the following dictionary for translating between the two sets of coefficients:

$$a_1 = -\tfrac{1}{2}d_2 - d_4, \qquad a_2 = \tfrac{1}{4}d_4, \qquad b_0 = 1 + \tilde{c}_2 + \tilde{c}_4, \quad b_1 = -\tfrac{1}{2}\tilde{c}_2 - \tilde{c}_4, \quad b_2 = \tfrac{1}{4}\tilde{c}_4, \tag{2.10}$$

where $(\tilde{c}_2, \tilde{c}_4)$ are the cosine–series coefficients of the numerator polynomial $1 + c_2\theta^2 + c_4\theta^4$. This allows us to design the shaper in the convenient Padé form and then directly implement it using the compact stencil.

With the shaper's form defined, the crucial task is to determine the optimal coefficients (c_2, c_4, d_2, d_4). Ideally, we would optimize the gain $g_A(\theta)$ over the entire spectral range $\theta \in [0, \pi]$. However, the limited degrees of freedom in the Padé(4,4) form preclude a perfect match to the ideal dispersion relation across the entire Nyquist range. Furthermore, optimizing for high wavenumbers often degrades performance in the well-resolved low wavenumbers. Therefore, we adopt a targeted optimization strategy based on a user-defined target resolution, or Points Per Wavelength (PPW). We define a cutoff wavenumber θ_c corresponding to this target limit:

$$\theta_c = \frac{2\pi}{\mathrm{PPW}}. \tag{2.11}$$

The fitting process is then split into two distinct regimes:

1. **Resolved Band ($0 \le \theta \le \theta_c$):** We rigorously minimize phase and group velocity errors to ensure high-fidelity transport.

2. **Unresolved Band ($\theta > \theta_c$):** We relax the accuracy requirements. Since high-wavenumber modes are dominated by truncation errors and are physically meaningless on the grid, they will be suppressed by the dissipation shaper (g_D) described in subsequent sections. Thus, for $\theta > \theta_c$, we only enforce the stability constraint $g_A(\theta) \le g_{A,\max}$ to prevent amplification.

To find the coefficients that satisfy these competing demands, we formulate a constrained weighted least–squares optimization problem. We minimize a cost function $J_A(\boldsymbol{x})$ over $\boldsymbol{x} = [c_2, c_4, d_2, d_4]$:

$$\min_{\boldsymbol{x}} \quad J_A(\boldsymbol{x}) = \sum_{\theta_k} W(\theta_k) \cdot \left[w_g \Big(c_g^{\boldsymbol{x}}(\theta_k) - c_{g,\mathrm{phys}} \Big)^2 + w_\phi \Big(c_\phi^{\boldsymbol{x}}(\theta_k) - c_{\phi,\mathrm{phys}} \Big)^2 \right], \tag{2.12}$$

$$\begin{aligned} \text{subject to} \quad & g_A(\theta; \boldsymbol{x}) \le g_{A,\max}, && \forall\, \theta \in [0, \pi], \\ & \mathrm{den}(\theta; \boldsymbol{x}) \ge \varepsilon, && \forall\, \theta \in [0, \pi], \end{aligned}$$

where $W(\theta)$ is a weighting function that is large ($W \gg 1$) for the resolved band $\theta \le \theta_c$ and small or zero for $\theta > \theta_c$. We solve (2.12) using a constrained optimization algorithm (e.g., Nelder–Mead [46]) to ensure the coefficients remain within the feasible region defined by the stability constraints. This approach ensures that the transport shaper focuses its limited capacity on the wavenumbers that actually matter for the simulation, relying on the dissipation mechanism to handle the unresolved scales.

To make the constrained optimization efficient, we provide an analytic initial guess for the Padé transport shaper coefficients using *low-angle moment matching*. Let the baseline reconstruction (transport) symbol be expanded about $\theta = 0$ as

$$\alpha(\theta) = \theta + a_3\theta^3 + a_5\theta^5 + \mathcal{O}(\theta^7), \tag{2.13}$$

where a_3 and a_5 are the leading dispersion-error coefficients of the chosen reconstruction. The Padé gain is

$$g_A(\theta) = \frac{1 + c_2\theta^2 + c_4\theta^4}{1 + d_2\theta^2 + d_4\theta^4} = 1 + A_2\theta^2 + A_4\theta^4 + \mathcal{O}(\theta^6), \tag{2.14}$$

with Taylor coefficients

$$A_2 = c_2 - d_2, \qquad A_4 = c_4 - d_4 - c_2 d_2 + d_2^2. \tag{2.15}$$

Enforcing maximum flatness of the shaped transport factor in the pass-band,

$$g_A(\theta)\,\alpha(\theta) = \theta + \mathcal{O}(\theta^5), \tag{2.16}$$

yields the moment constraints

$$A_2 = -a_3, \qquad A_4 = -a_5 + a_3^2, \tag{2.17}$$

so the seed parameters can be obtained directly from (a_3, a_5). We use two practical strategies:

- **MN (Matches Numerator):** set $d_2 = d_4 = 0$, so $c_2 = A_2$ and $c_4 = A_4$.
- **BD (Both Denominator):** choose (d_2, d_4) (typically $d_2 > 0$, $d_4 = 0$) to improve bounded-gain behavior, then set $c_2 = d_2 + A_2 = d_2 - a_3$ and $c_4 = A_4 + d_4 + d_2 A_2 = (-a_5 + a_3^2) + d_4 - a_3 d_2$.

In practice, BD seeds keep the denominator active and typically satisfy the gain constraint $(g_{A,\max})$ with fewer optimizer iterations.

Practical seeds for reconstructions used in this thesis.

$$\begin{aligned}
\textbf{CD2:}\ & \alpha = \sin\theta = \theta - \tfrac{1}{6}\theta^3 + \tfrac{1}{120}\theta^5 + \cdots \\
& \Rightarrow \text{MN: } d_2 = d_4 = 0,\ c_2 = \tfrac{1}{6},\ c_4 = \tfrac{7}{360}, \\
& \Rightarrow \text{BD: } d_2 = \tfrac{1}{18},\ d_4 = 0,\ c_2 = \tfrac{2}{9},\ c_4 = \tfrac{7}{360} - \tfrac{1}{324} + \tfrac{2}{162}. \\
\textbf{CD4/MUSCL3:}\ & \alpha = \tfrac{8\sin\theta - \sin 2\theta}{6} = \theta - \tfrac{1}{30}\theta^5 + \cdots \\
& \Rightarrow \text{MN: } d_2 = d_4 = 0,\ c_2 = 0,\ c_4 = \tfrac{1}{30}, \\
& \Rightarrow \text{BD: } c_2 = d_2,\ d_4 = 0,\ c_4 = \tfrac{1}{30}. \\
\textbf{MUSCL2 (BW):}\ & \alpha = (2 - \cos\theta)\sin\theta = \theta + \tfrac{1}{3}\theta^3 - \tfrac{7}{60}\theta^5 + \cdots \\
& \Rightarrow \text{MN: } d_2 = d_4 = 0,\ c_2 = -\tfrac{1}{3},\ c_4 = \tfrac{41}{180}, \\
& \Rightarrow \text{BD: } d_2 = \tfrac{1}{3},\ d_4 = 0,\ c_2 = 0,\ c_4 = \tfrac{7}{60}.
\end{aligned}$$

In summary, this bounded Padé transport shaper, realized compactly on flux paths, provides an elegant and powerful mechanism for high-fidelity simulations. It delivers exact, local spectral control, cancels the dominant transport errors of the underlying reconstruction, avoids numerical instabilities through bounded gain and denominator positivity, and remains efficient and boundary-friendly without relying on global transforms.

2.4 Diffusion shaper: monotone spectral bump

Having addressed dispersion on the transport path, we now turn to the *diffusive path*. Here, our goal is not to eliminate dissipation entirely, but to control it precisely. We introduce a second filter, the diffusion shaper $g_D(\theta)$, which acts as a programmable "dimmer switch" for the numerical damping native to the solver. This shaper is designed as a real-even, nondecreasing "spectral bump" function:

$$g_D(\theta) \;=\; r_{\text{pass}} + (r_{\text{high}} - r_{\text{pass}})\,\frac{z^{2q}}{1+z^{2q}}, \qquad z = \frac{\max(0,\theta-\theta_t)}{\pi-\theta_t}, \qquad q \in \{4,6\}. \tag{2.18}$$

This function smoothly transitions the damping level from r_{pass} in the pass band to r_{high} at the highest wavenumbers. By construction, $g_D(\theta)$ is always nonnegative and monotone (nondecreasing) in θ. This is a critical safety feature: it guarantees that the shaper can never accidentally add energy to the simulation by flipping the sign of the modal damping, thus preventing destabilization. This design ensures that dissipation control remains fully decoupled from the transport tuning performed earlier.

The parameter $q > 0$ sets the *smoothness/steepness* of the transition (larger q yields a more drastic roll-off), and θ_t is the *dissipation threshold* that marks the onset of the transition. Ideally, θ_t is chosen based on the target resolution (PPW). While it is often set close to the transport cutoff θ_c (defined in Sec. 2.3) to maximize the useful bandwidth, θ_t remains an independent parameter. This decoupling allows the user to fine-tune the spectral window where dissipation is active, distinct from where dispersion errors are corrected.

In smooth flow regions, we configure the shaper for Zero Pass-Band Dissipation (ZPD) to satisfy requirement R6. By setting the pass-band level to $r_{\text{pass}} = 0$ and choosing

an appropriate threshold θ_t (typically $\theta_t \approx 2\pi/\text{PPW}$), we ensure that $g_D(\theta) \approx 0$ for all well-resolved waves. This leaves the physically relevant spectrum pristine, while the monotone rise to r_{high} in the high wavenumbers maintains background stability. Conversely, in the presence of discontinuities, the method prioritizes Shock Robustness (R7). A sensor-based gating mechanism acts as a safety bypass, forcing $g_D = 1$ where shocks are detected. This instantly recovers the full, unmodified dissipation of the baseline shock-capturing solver, thereby preserving the proven shock thickness and nonlinear stability of the underlying scheme without user intervention.

For computational efficiency and consistency, we implement the diffusion shaper with the *same* compact Padé operator used for transport. Given a target spectral response

$$g(\theta) = \frac{b_0 + 2b_1 \cos\theta + 2b_2 \cos 2\theta}{1 + 2a_1 \cos\theta + 2a_2 \cos 2\theta}, \tag{2.19}$$

we apply the following *pentadiagonal* compact relation to the diffusive flux:

$$Y_j + a_1(Y_{j-1} + Y_{j+1}) + a_2(Y_{j-2} + Y_{j+2}) = b_0 X_j + b_1(X_{j-1} + X_{j+1}) + b_2(X_{j-2} + X_{j+2})\,, \tag{2.20}$$

where $\{X_j\}$ and $\{Y_j\}$ denote the unshaped and shaped *diffusive* fluxes. In matrix form this is $A_p Y = B_p X$ with a five-diagonal A_p, which we solve by a banded direct method in $O(N)$ work per variable. This enforces the desired $g(\theta)$ on the dissipation pathway—reducing or redistributing damping in the passband while allowing growth toward high wavenumbers for shock robustness.

The diffusion gain is prescribed as a *monotone bump* $g_D(\theta)$ with a distinct onset threshold θ_t. We then determine the Padé$(4,4)$ coefficients $\boldsymbol{x} = [c_2, c_4, d_2, d_4]$ for the operator

$$g(\theta; \boldsymbol{x}) = \frac{1 + c_2\theta^2 + c_4\theta^4}{1 + d_2\theta^2 + d_4\theta^4}, \tag{2.21}$$

by minimizing a weighted least–squares mismatch between the implementable gain $g(\theta; \boldsymbol{x})$ and the target $g_D(\theta)$ on $[0, \pi]$. The weighting function is designed to enforce strict adherence to the ZPD condition in the passband ($0 \le \theta \le \theta_t$) while allowing the bump profile to develop in the high-wavenumber range. Simple penalties cap the gain and keep the Padé denominator away from zero; the search is performed with a

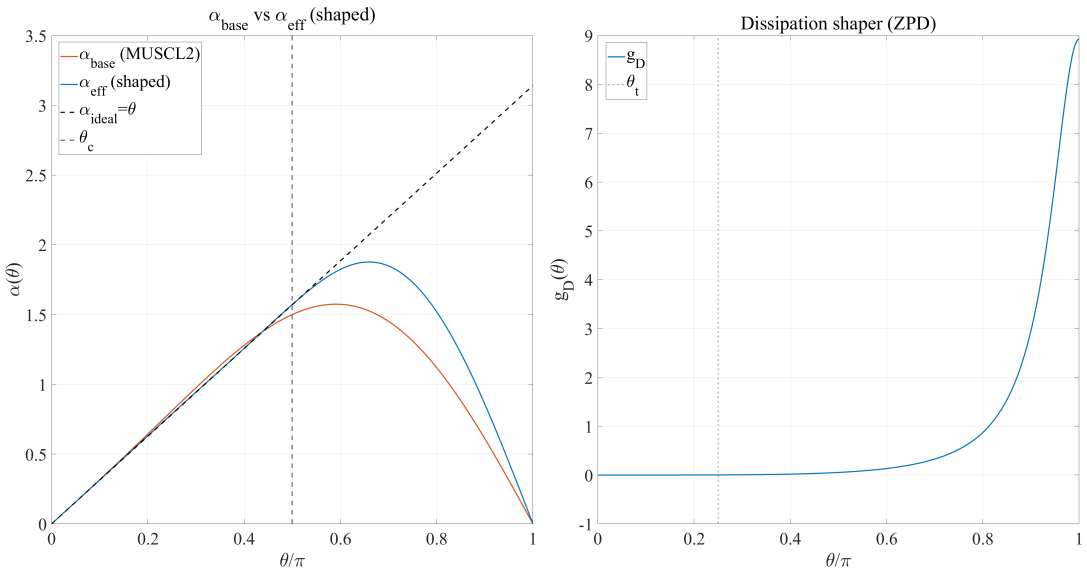

Figure 2.1: Spectral response of the optimized compact shapers. *Left:* Effective dispersion $\alpha_{\text{eff}}(\theta)$; the shaped scheme (blue) significantly extends the linear bandwidth compared to MUSCL2 (Beam–Warming) (red). *Right:* Dissipation gain $g_D(\theta)$ illustrating the ZPD property, where damping is negligible below θ_t and rises sharply thereafter for stability.

derivative–free Nelder–Mead method. The resulting coefficients are used in (2.20) to realize the monotone bump on the diffusive paths.

Figure 2.1 illustrates the spectral characteristics of the optimized shapers. The left panel demonstrates the efficacy of the transport shaper (g_A): the effective modified wavenumber α_{eff} of the shaped scheme tracks the ideal line $\alpha = \theta$ much further into the spectrum than the baseline MUSCL2 scheme, directly translating to reduced phase errors. The right panel confirms the ZPD property of the dissipation shaper (g_D), showing virtually zero gain in the resolved low-wavenumber region ($\theta < \theta_t$) and a controlled rise in the unresolved high-wavenumber range.

2.5 Semi-discrete Symbol and Scheme Guarantees

With the shapers for the transport and diffusive paths designed, we now analyze the behavior of the complete, modified scheme. The two shapers (g_A and g_D) are applied as compact, real-even gains to their respective flux paths. The result is a powerful analytical tool: the semi-discrete eigenvalue (or symbol), $\lambda_{\text{sd}}(\theta)$, which acts as the complete mathematical "fingerprint" of our final scheme for a single wave of frequency

θ. This eigenvalue is the sum of the shaped transport and diffusive contributions:

$$\lambda_{\mathrm{sd}}(\theta) = \underbrace{\frac{\mathrm{i}}{h} g_A(\theta)\alpha(\theta)}_{\text{Imaginary Part: Wave Propagation}} \underbrace{-\frac{1}{h} g_D(\theta)\mu_0(\theta)}_{\text{Real Part: Damping}}, \tag{2.22}$$

where $\alpha(\theta)$ is the reconstruction's transport factor and $\mu_0(\theta)$ is the solver's baseline modal damping. From this, we can directly compute the scheme's effective phase speed (c_ϕ) and group velocity (c_g):

$$c_\phi(\theta) = \frac{\Im\,\lambda_{\mathrm{sd}}(\theta)}{k}, \qquad c_g(\theta) = \frac{\partial\,\Im\,\lambda_{\mathrm{sd}}}{\partial k}, \qquad k = \theta/h. \tag{2.23}$$

Based on this spectral formulation, we can systematically verify that the SFS-FVM formulation satisfies essential physical and numerical requirements. We begin by establishing the method's physical consistency, specifically its ability to conserve mass and energy and to correctly maintain uniform flow states.

Proposition 1 (Conservation and freestream)**.** *Let $g_A(\theta)$ be real-even with $g_A(0) = 1$ on transport paths. Then the shaped transport flux has the same DC mode as the unshaped one, and the discrete divergence of a constant flux remains zero. Applying g_D to a zero-mean dissipative path preserves mean conservation. Therefore the FV update (2.1) remains conservative and freestream-preserving.*

Proof. If the face flux is constant, its spectrum is supported at $\theta = 0$, hence $\widehat{Y}(0) = g_A(0)\widehat{X}(0) = \widehat{X}(0)$. The shaped face difference $Y_{i+\frac{1}{2}} - Y_{i-\frac{1}{2}}$ is identically zero, so the discrete divergence vanishes. Mean conservation on the dissipative path holds since g_D acts on a zero-mean quantity. □

Next, to ensure robust performance, we verify that the shaping process does not introduce numerical instabilities. A critical safety feature of our design is the guarantee that the diffusion shaper functions strictly as a damper and cannot accidentally inject energy into the simulation.

Proposition 2 (Nonnegative modal damping preserved)**.** *Let $\mu_0(\theta) \geq 0$ denote the baseline diffusive modal damping for a given path. If $g_D(\theta) \geq 0$ for all θ, then the shaped*

damping $\mu(\theta) = g_D(\theta)\mu_0(\theta)$ *is also nonnegative. Hence shaping cannot destabilize a diffusion-stable block.*

We also confirm that the transport path itself is well-behaved. To avoid amplifying numerical noise during the dispersion-correction process, the optimization procedure strictly constrains the shaper's gain.

Remark 1 (Bounded transport amplification)**.** Because the Padé denominator is kept strictly positive (diagonal-dominant compact system, cf. (2.7)) and the fit penalizes excess gain (cf. (2.12)), the transport shaper satisfies $g_A(\theta) \le g_{A,\max}$ and the compact solve is well-conditioned. This prevents energy blow-up on the transport path.

Finally, we address the primary design goal of high-fidelity acoustic propagation. The following proposition formally proves that when the Zero Pass-Band Dissipation (ZPD) condition is applied to the AUSM+up solver, the method achieves perfect, undamped wave propagation for all well-resolved frequencies.

Proposition 3 (Passband zero-damping property)**.** *Consider a flux splitting of AUSM +up or Roe type on a uniform grid with smooth data. If the diffusion shaper satisfies* $g_D(\theta) \equiv 0$ *for* $\theta \in [0, \theta_c]$*, then the semi-discrete eigenvalues of the resulting discretization are purely imaginary in the passband, i.e.,*

$$\Re[\lambda_{\mathrm{sd}}(\theta)] = 0, \qquad \forall\, \theta \in [0, \theta_c]. \tag{2.24}$$

Proof. In both AUSM +up and Roe flux splittings, the only real (damping) contribution arises from the upwind or diffusive flux components (e.g., the pressure-diffusion term in AUSM +up or the jump term in Roe). Multiplying this diffusive path by $g_D(\theta) = 0$ nullifies its contribution on $[0, \theta_c]$, while the remaining central advective and pressure components contribute only imaginary eigenvalues. Hence the semi-discrete operator is nondissipative within the passband, satisfying $\Re\, \lambda_{\mathrm{sd}}(\theta) = 0$ for $\theta \in [0, \theta_c]$. □

2.6 Sensor-Based Gating and Final Shaped Flux Formulation

This section details the practical machinery that enables the scheme to adapt to the local flow, applying high-fidelity shaping in smooth regions while reverting to a

robust shock-capturing mode near discontinuities. This is achieved through a multi-stage process of sensing, smoothing, gating, and careful calibration.

2.6.1 Shock Sensor Design

First, we design a sensor, S, which acts as the "eyes" of the scheme. To ensure robustness, the sensor combines two distinct physical indicators. The primary component is a curvature-based indicator inspired by the Effective Scaled Wavenumber (ESW) concept. For any scalar quantity q, we define the first and second differences as $\delta q_i = \frac{1}{2}(q_{i+1} - q_{i-1})$ and $\Delta q_i = q_{i+1} - 2q_i + q_{i-1}$. Using these, we form a curvature indicator from density and pressure:

$$\kappa_i = \max\left(\frac{|\Delta\rho_i|}{|\delta\rho_i| + \varepsilon}, \frac{|\Delta p_i|}{|\delta p_i| + \varepsilon}\right), \quad S_i^{\mathrm{ESW}} = \mathrm{clip}\left(\frac{\kappa_i - k_c}{k_{\max} - k_c}, 0, 1\right), \tag{2.25}$$

with $\varepsilon = 10^{-12}$, $k_c \in [0.8, 0.95]$, and $k_{\max} \in [2.0, 2.5]$. This is supplemented by a direct measure of the pressure jump across each face:

$$S_{i+\frac{1}{2}}^{\Delta p} = 1 - \exp\left[-C_{\mathrm{sh}}\left(\frac{|p^R - p^L|}{\mathrm{median}_\Omega p}\right)^2\right], \quad C_{\mathrm{sh}} \in [40, 100]. \tag{2.26}$$

The raw sensor value at the face is the maximum of these two indicators: $S_{i+\frac{1}{2}}^{\mathrm{raw}} = \max(S_{i+\frac{1}{2}}^{\mathrm{ESW}}, S_{i+\frac{1}{2}}^{\Delta p})$.

2.6.2 Halo Smoothing and Gating Function

To ensure stability near strong discontinuities, it is critical to deactivate shaping not just at the shock itself but also in a small neighborhood around it. We achieve this by applying a maximum-filter (halo) of width n_{halo} (typically 1–5 cells):

$$S_{i+\frac{1}{2}}^{\mathrm{sm}} = \max_{j \in [i - n_{\mathrm{halo}}, i + n_{\mathrm{halo}}]} \left(S_{j+\frac{1}{2}}^{\mathrm{raw}}\right). \tag{2.27}$$

Finally, to prevent background noise from triggering the switch, we apply a threshold S_0 (typically 0.002) and a power-law mapping to obtain the final shock weight $w_{\text{shock}} \in [0, 1]$:

$$\tau = \text{clip}\left(\frac{S^{\text{sm}}_{i+\frac{1}{2}} - S_0}{1 - S_0}, 0, 1\right), \qquad w_{\text{shock}} = \tau^{\kappa}, \quad \kappa \in [0.05, 0.4]. \tag{2.28}$$

Here, $w_{\text{shock}} = 1$ corresponds to full shock capturing (Unshaped), and $w_{\text{shock}} = 0$ enables full spectral shaping.

In the implementation, the gate is applied by *linear blending* between the unshaped and shaped fluxes. For any flux contribution $\mathbf{F}$ and its shaped counterpart $\mathbf{F}^{\text{sh}}$ (obtained by applying the compact Padé operator), the gated flux is

$$\mathbf{F} \leftarrow w_{\text{shock}}\,\mathbf{F} + (1 - w_{\text{shock}})\,\mathbf{F}^{\text{sh}}. \tag{2.29}$$

For a single Fourier mode this is equivalent to an *effective gain*

$$g_{\text{eff}}(\theta; S) = 1 + (1 - w_{\text{shock}}(S))\Big(g(\theta) - 1\Big). \tag{2.30}$$

Thus, the transport and diffusion paths act with

$$g_{A,\text{eff}}(\theta; S) = 1+(1-w_{\text{shock}}(S))\Big(g_A(\theta)-1\Big), \qquad g_{D,\text{eff}}(\theta; S) = 1+(1-w_{\text{shock}}(S))\Big(g_D(\theta)-1\Big). \tag{2.31}$$

These weights act like a sharp crossfader. A subtle challenge is that the shapers (g_A, g_D) are designed in Fourier space, whereas the sensor S operates in physical space. To ensure compatibility, we calibrate the shapers on pure sine waves where the sensor activity is negligible, then freeze the coefficients for use in complex flows. For efficiency, the sensor S is computed only once per time step and reused across all Runge–Kutta stages.

Roe. For the Roe solver, we separate the numerical flux into a central (transport) part and a dissipative part, $\widehat{\mathbf{F}} = \mathbf{F}^{\text{c}} + (-\mathbf{D})$. Each part is then shaped and gated using

(2.29):

$$\mathbf{F}^{\mathrm{c}} \leftarrow w_{\mathrm{shock}}\,\mathbf{F}^{\mathrm{c}} + (1 - w_{\mathrm{shock}})\,\mathbf{F}^{\mathrm{c,sh}}, \tag{2.32}$$

$$(-\mathbf{D}) \leftarrow w_{\mathrm{shock}}\,(-\mathbf{D}) + (1 - w_{\mathrm{shock}})\,(-\mathbf{D})^{\mathrm{sh}}, \tag{2.33}$$

$$\widehat{\mathbf{F}} = \mathbf{F}^{\mathrm{c}} + (-\mathbf{D}). \tag{2.34}$$

For additional stability near strong shocks, a small Local Lax–Friedrichs (LLF) floor may be blended in where the sensor indicates a discontinuity.

AUSM+up. For AUSM+up we use the flux-path separation $\widehat{\mathbf{F}} = \widehat{\mathbf{F}}^{\mathrm{adv}} + \widehat{\mathbf{F}}^{\mathrm{press}} + \widehat{\mathbf{F}}^{\mathrm{UP}}$. Both the transport-dominated and upwind (diffusive) contributions are gated with the same shock gate:

$$\widehat{\mathbf{F}}^{\mathrm{adv}} + \widehat{\mathbf{F}}^{\mathrm{press}} \leftarrow w_{\mathrm{shock}}\left(\widehat{\mathbf{F}}^{\mathrm{adv}} + \widehat{\mathbf{F}}^{\mathrm{press}}\right) + (1 - w_{\mathrm{shock}})\left(\widehat{\mathbf{F}}^{\mathrm{adv}} + \widehat{\mathbf{F}}^{\mathrm{press}}\right)^{\mathrm{sh}}, \tag{2.35}$$

$$\widehat{\mathbf{F}}^{\mathrm{UP}} \leftarrow w_{\mathrm{shock}}\,\widehat{\mathbf{F}}^{\mathrm{UP}} + (1 - w_{\mathrm{shock}})\left(\widehat{\mathbf{F}}^{\mathrm{UP}}\right)^{\mathrm{sh}}, \tag{2.36}$$

$$\widehat{\mathbf{F}} = \left(\widehat{\mathbf{F}}^{\mathrm{adv}} + \widehat{\mathbf{F}}^{\mathrm{press}}\right) + \widehat{\mathbf{F}}^{\mathrm{UP}}. \tag{2.37}$$

2.7 Algorithmic Blueprint

The sequence of operations performed at each stage of the Runge–Kutta time integration can be expressed as a formal algorithm. The core procedure is to compute the shaped numerical flux, $\widehat{\mathbf{F}}$, at every cell interface, and then use these fluxes to compute the semi-discrete time derivative, $\mathrm{d}\mathbf{U}/\,\mathrm{d}t$.

Algorithm 1 Shaped Flux Calculation (Single RK Stage)

Require: State vector field $\mathbf{U}$ at current stage.

Ensure: Semi-discrete time derivative $\mathrm{d}\mathbf{U}/\,\mathrm{d}t$.

procedure ComputeShapedFluxDivergence($\mathbf{U}$)

Phase 1: Sensor construction and Gating

Compute cell curvature indicator κ_i from ρ, p using $\delta(\cdot), \Delta(\cdot)$.

Convert to face ESW sensor $S^{\mathrm{ESW}}_{i+\frac{1}{2}}$ (e.g., max of adjacent cells).

Reconstruct primitive pressures (p^L, p^R) on faces using a robust stencil (e.g., CD2).

Compute pressure-jump sensor $S^{\Delta p}_{i+\frac{1}{2}}$ and set raw sensor $S^{\mathrm{raw}}_{i+\frac{1}{2}} = \max(S^{\mathrm{ESW}}_{i+\frac{1}{2}}, S^{\Delta p}_{i+\frac{1}{2}})$.

Apply Halo: $S_{i+\frac{1}{2}} \leftarrow \max_{j\in\mathrm{halo}} S^{\mathrm{raw}}_{j+\frac{1}{2}}$ to widen the protected region.

Compute shock gate w_{shock} using threshold S_0 and exponent κ:

$\tau \leftarrow \mathrm{clip}\big((S_{i+\frac{1}{2}} - S_0)/(1 - S_0),\, 0,\, 1\big)$,

$w_{\mathrm{shock}} \leftarrow \tau^{\kappa}, \quad$ with $\kappa \in [0.05, 0.4]$.

(Note) $w_{\mathrm{shock}} \to 1$ recovers baseline; $w_{\mathrm{shock}} \to 0$ applies full shaping.

Phase 2: Reconstruction for flux evaluation

Reconstruct face states $\mathbf{U}^L, \mathbf{U}^R \leftarrow \mathrm{Reconstruct}(\mathbf{U})$ (with chosen limiter).

Phase 3: Flux decomposition (path separation)

for all interior faces $i + \frac{1}{2}$ **do**

  if solver is Roe **then**

    $\mathbf{F}^{\mathrm{c}} \leftarrow \frac{1}{2}\Big(\mathbf{F}(\mathbf{U}^L) + \mathbf{F}(\mathbf{U}^R)\Big)$

    $(-\mathbf{D}) \leftarrow$ Roe viscous flux (with entropy fix / eigenvalue floor)

  else if solver is AUSM+up **then**

    $\mathbf{F}^{\mathrm{adv}}, \mathbf{F}^{\mathrm{press}}, \mathbf{F}^{\mathrm{UP}} \leftarrow$ AUSM+up split

    (optional) adapt (K_p, K_u) and/or LLF blending strength using S

Phase 4: Spectral shaping + gating (implemented as blending)

Compute shaped transport flux: $\mathbf{F}^{\mathrm{c}}_{\mathrm{sh}} \leftarrow g_A \odot \mathbf{F}^{\mathrm{c}}$ (or $g_A \odot (\mathbf{F}^{\mathrm{adv}} + \mathbf{F}^{\mathrm{press}})$).

Compute shaped diffusive flux: $\mathbf{D}_{\mathrm{sh}} \leftarrow g_D \odot (-\mathbf{D})$ (or $g_D \odot \mathbf{F}^{\mathrm{UP}}$).

Gate by blending on each face:

$\mathbf{F}^{\mathrm{c}} \leftarrow w_{\mathrm{shock}}\,\mathbf{F}^{\mathrm{c}} + (1 - w_{\mathrm{shock}})\,\mathbf{F}^{\mathrm{c}}_{\mathrm{sh}}, \quad (-\mathbf{D}) \leftarrow w_{\mathrm{shock}}\,(-\mathbf{D}) + (1 - w_{\mathrm{shock}})\,\mathbf{D}_{\mathrm{sh}}$.

Phase 5: Reassembly & divergence

for all cells i **do**

  if solver is Roe **then**

    $\widehat{\mathbf{F}}_{i\pm\frac{1}{2}} \leftarrow \mathbf{F}^{\mathrm{c}}_{i\pm\frac{1}{2}} + (-\mathbf{D})_{i\pm\frac{1}{2}}$

  else if solver is AUSM+up **then**

    $\widehat{\mathbf{F}}_{i\pm\frac{1}{2}} \leftarrow (\mathbf{F}^{\mathrm{adv}} + \mathbf{F}^{\mathrm{press}})_{i\pm\frac{1}{2}} + \mathbf{F}^{\mathrm{UP}}_{i\pm\frac{1}{2}}$

  $(\,\mathrm{d}\mathbf{U}/\,\mathrm{d}t)_i \leftarrow -\frac{1}{h}\left(\widehat{\mathbf{F}}_{i+\frac{1}{2}} - \widehat{\mathbf{F}}_{i-\frac{1}{2}}\right)$

return $\mathrm{d}\mathbf{U}/\,\mathrm{d}t$

Chapter 3

Results

This chapter evaluates the proposed flux-shaped schemes, hereafter referred to as *Shaped*, against their unmodified baseline counterparts, referred to as *Vanilla*. The assessment is organized into three complementary categories:

(i) *Fundamental wave propagation:* These unit tests quantify linear dispersion and dissipation errors using 1-D Gaussian wave packets and 2-D angle sweeps. Performance is tracked via the complex modal amplitude $a^+(t; k_0)$ of the forward-traveling branch to assess transport fidelity and directional isotropy.

(ii) *Nonlinear robustness:* These problems involve strong shocks (Sod, Shu-Osher) to verify stability and shock-capturing capability. Accuracy is quantified using L_1 error norms to demonstrate that the shaping mechanism maintains high fidelity without inducing instability. Additionally, the discrete Rankine-Hugoniot (RH) residuals are monitored to verify that the method strictly satisfies conservation laws across discontinuities.

(iii) *Pulse propagation in a mean flow:* This benchmark simulates the simultaneous convection of acoustic, entropy, and vorticity pulses in a uniform mean flow. It evaluates the scheme's fidelity in preserving pulse shapes and maintaining directional isotropy over long integration times.

For all simulations, the governing equations are the compressible Euler equations, and the working fluid is an ideal gas with $\gamma = 1.4$. To ensure reproducibility and concise presentation, the numerical configuration for each test case is summarized in Table 3.1.

3.1 1-D Gaussian Wave Packet Advection

To validate the fundamental linear transport properties of the proposed scheme, we simulate the advection of a 1-D Gaussian wave packet. This problem isolates the

Table 3.1: Summary of numerical configurations for validation test cases.

Test Case	Resolution / Grid	Reconstruction	Flux Scheme	Time Integration
Fundamental Wave Propagation				
1-D Gaussian Advection	PPW = 6	MUSCL3 (QUICK)	AUSM+up	RK4, CFL = 0.1
2-D Contact Sweep	PPW = 6	MUSCL3 (QUICK)	AUSM+up	RK4, CFL = 0.1
2-D Acoustic Sweep	PPW = 8	CD2	Roe	RK4, CFL = 0.12
Nonlinear Robustness				
1-D Shock Tube (Sod)	$N = 400$	MUSCL2 (Fromm)	Roe / AUSM+up	RK4, CFL = 0.2
Shu-Osher Interaction	$N = 1024$	MUSCL2 (Fromm)	Roe / AUSM+up	RK4, CFL = 0.2
Pulse Propagation in Mean Flow				
Acoustic, Entropy, and Vorticity Pulses	1200×1200	MUSCL2 (Beam–Warming)	AUSM+up	RK4, CFL = 0.1

scheme's ability to preserve the *phase velocity (dispersion)* and *amplitude (dissipation)* of acoustic waves in a simple convective environment, free from multi-dimensional effects or complex boundary interactions.

The background flow is uniform with a mean velocity $u_\infty = 0.2$ and sound speed $c_\infty = 1.0$ (Mach number $M_\infty = 0.2$). The initial perturbation is defined as a right-running acoustic wave (characteristic speed $u + c$) with a small amplitude $A = 5 \times 10^{-6}$ to ensure the system remains in the linear regime.

The wave packet is constructed by modulating a carrier wave with a Gaussian envelope:

$$\rho'(x, 0) = A \exp\left[-\frac{1}{2}\left(\frac{x}{\sigma_L}\right)^2\right] \cos(k_0 x), \tag{3.1}$$

where the carrier wavenumber is set to $k_0 = 2\pi m/L$, corresponding to a target resolution of PPW (Points Per Wavelength) ≈ 6. Specifically, the carrier wavelength is defined as $\lambda_0 = 2\pi/k_0 = 6h$, where h is the grid spacing. This choice of PPW represents a marginally resolved scale often encountered in practical aeroacoustic simulations, where high-order schemes typically struggle. The envelope width is set to $\sigma_L = 2\lambda_0$ to localize the packet in physical space. The exact physical propagation speed of this acoustic mode is $c_{\text{exact}} = u_\infty + c_\infty = 1.2$.

Table 3.2: Quantitative errors for the carrier wave ($k_0 \Delta x \approx \pi/3$) at PPW=6.

Scheme	**Dispersion Error (%)**	**Nondimensional Dissipation** ($\mu h/\lvert\lambda\rvert$)
Unshaped	-2.805	0.0495
Shaped	-0.236	0.0000

Quantitative results for the carrier frequency are summarized in Table 3.2. The

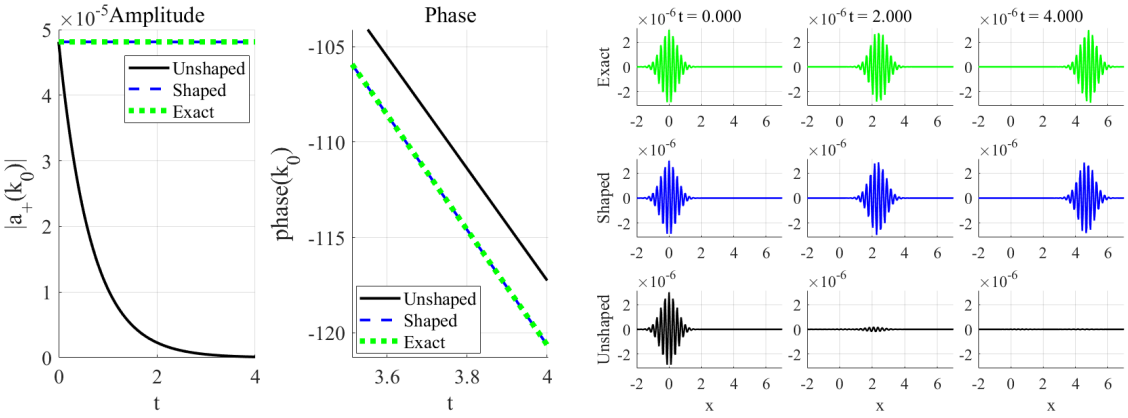

Figure 3.1: Gaussian packet diagnostics comparing *Unshaped* and *Shaped* schemes at a carrier resolution of PPW=6 ($\lambda_0 = 6h$). *Method:* MUSCL3 reconstruction with AUSM+up flux. The left panel tracks the modal amplitude $|A(t)|$ and cumulative phase $\phi(t)$ of the carrier component k_0. The right panel visualizes the spatial evolution of the density perturbation $\rho'(x,t)$ at $t = 0, 2, 4$, demonstrating the preservation of the wave envelope.

Shaped scheme reduces the dispersion error by over an order of magnitude compared to the baseline (Unshaped) and effectively eliminates numerical dissipation in the pass-band range.

As shown in the time-history plots (Figure 3.1), the *Shaped* scheme maintains a near-constant modal amplitude and accurately tracks the exact linear phase evolution. This confirms that the spectral shaping successfully enforces the Zero Pass-Band Dissipation (ZPD) condition and corrects the phase lag inherent in the base scheme. Conversely, the *Unshaped* scheme exhibits significant amplitude decay and cumulative phase error (lag), causing the wave packet to diffuse and drift downstream slower than the physical speed. This is visually corroborated by the snapshots, where the *Shaped* solution preserves the pulse envelope's shape and position over long-distance propagation, whereas the baseline solution is visibly damped and dispersed.

3.2 2-D Oblique Contact Wave Advection (Angle Sweep)

In multi-dimensional simulations, the numerical error of finite volume schemes is often highly dependent on the direction of wave propagation relative to the grid lines. Standard dimension-by-dimension reconstruction approaches typically exhibit minimal error when the flow is aligned with the grid axes $(0°, 90°)$ but suffer from maximum

dissipation and dispersion error at oblique angles (e.g., 45°). To assess the directional isotropy of the proposed scheme, we simulate the advection of a 2-D contact (entropy) wave across a range of propagation angles.

The background flow is uniform with velocity $\mathbf{U}_\infty = (0.3, 0.2)$, pressure $p_\infty = 1.0$, and density $\rho_\infty = 1.0$. The initial condition consists of a Gaussian-modulated density perturbation with amplitude $A = 0.1$, while pressure and velocity are kept constant to isolate the entropy mode:

$$\rho'(x, y, 0) = A \exp\left[-\frac{1}{2}\left(\frac{\mathbf{n} \cdot \mathbf{x}}{\sigma_L}\right)^2\right] \cos(\mathbf{k}_0 \cdot \mathbf{x}), \tag{3.2}$$

where $\mathbf{x} = (x, y)$, and the carrier wave vector is defined as $\mathbf{k}_0 = (k_x, k_y) = |\mathbf{k}_0|(\cos\theta, \sin\theta)$. The propagation angle θ is swept from 0° to 180°. The target resolution is fixed at PPW ≈ 6, meaning the carrier wavelength $\lambda_0 = 2\pi/|\mathbf{k}_0|$ is resolved by approximately 6 grid points regardless of the angle. The exact physical phase speed of this wave is the projection of the flow velocity onto the wave vector:

$$c_{\phi,\text{exact}}(\theta) = \frac{\mathbf{k}_0 \cdot \mathbf{U}_\infty}{|\mathbf{k}_0|} = U_\infty \cos\theta + V_\infty \sin\theta. \tag{3.3}$$

We track the evolution of the complex mode amplitude $a(t; \mathbf{k}_0)$ using a Lagrangian moving window to minimize boundary effects. The numerical phase speed $c_{\phi,\text{num}}$ and damping rate μ are computed via:

$$c_{\phi,\text{num}} = \frac{1}{|\mathbf{k}_0|}\frac{d}{dt}\arg a(t), \qquad \mu = -\frac{d}{dt}\ln|a(t)|. \tag{3.4}$$

Figure 3.2 presents the results of the angular sweep. The bottom row clearly illustrates the grid anisotropy inherent in the *Vanilla* scheme; the phase error and dissipation rate fluctuate significantly depending on θ, with peak errors occurring at oblique angles. In contrast, the *Shaped* scheme accurately tracks the exact theoretical phase speed across all propagation angles, effectively eliminating the angular deviations observed in the baseline scheme. Furthermore, it yields a nearly flat, near-zero damping

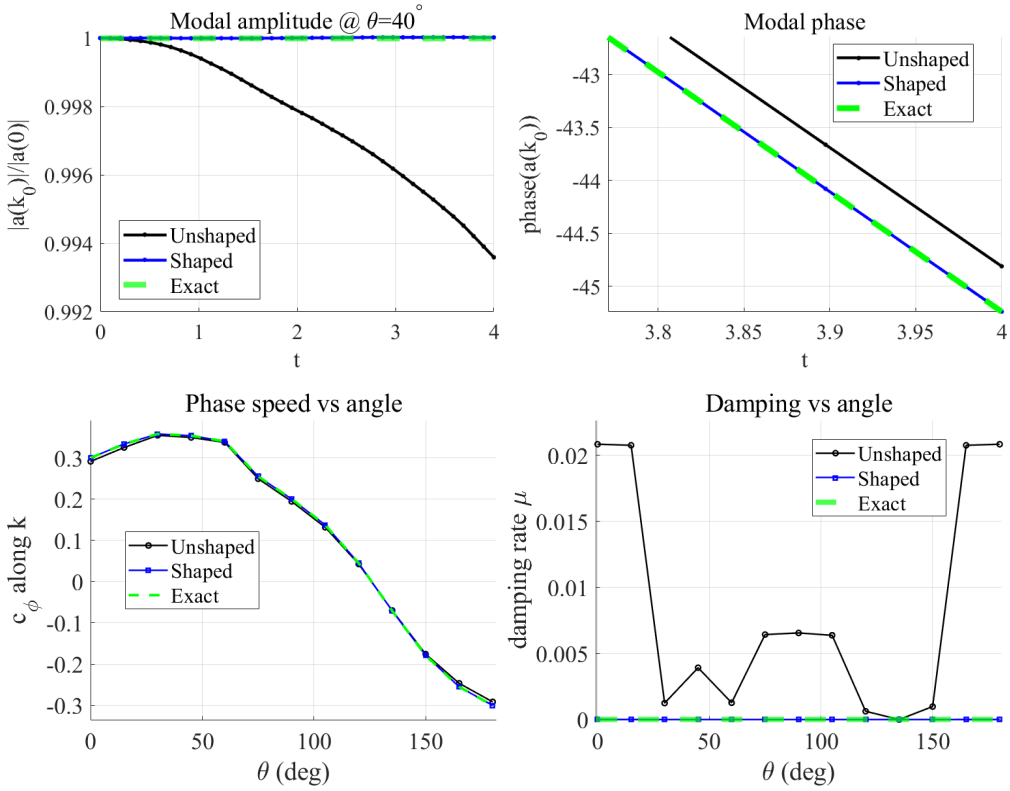

Figure 3.2: Diagnostics for the 2-D nonlinear contact wave at PPW=6. *Method:* MUSCL3 reconstruction with AUSM+up flux. Top row: Time evolution of the normalized modal amplitude (left) and unwrapped phase (right) for a specific propagation angle of $\theta = 40°$. Bottom row: Results of the angular sweep showing Phase speed c_ϕ (left) and Damping rate μ (right) as a function of propagation angle θ. The *Shaped* scheme demonstrates superior isotropy compared to the *Unshaped* scheme.

profile, demonstrating superior isotropy. These results confirm that the spectral shaping effectively restores isotropic transport properties and validates the ZPD design for multi-dimensional scalar transport, ensuring that waves propagate with consistent fidelity regardless of grid orientation.

This spectral behavior is corroborated spatially in Figure 3.3 for the $\theta = 40°$ case. The error field of the *Unshaped* scheme is dominated by coherent, anisotropic wave structures trailing the pulse center. These structures correspond directly to the dispersive phase lag identified in Figure 3.2. Conversely, the *Shaped* scheme significantly suppresses these structured dispersion errors. The remaining error field consists of low-amplitude, unstructured noise, confirming that the scheme accurately preserves the shape and position of the entropy pulse during multi-dimensional convection.

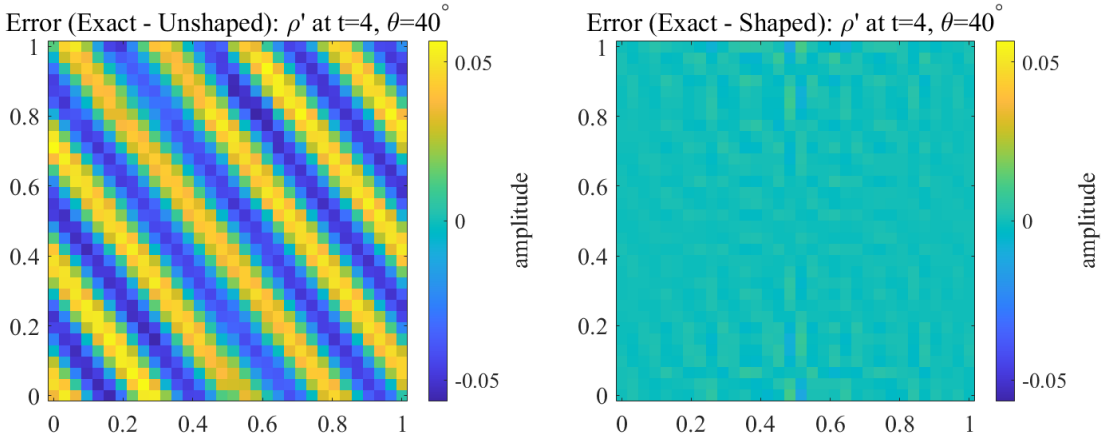

Figure 3.3: Spatial error distribution of the density perturbation ($\rho_{\text{exact}} - \rho_{\text{num}}$) at $t = 4.0$ for the $\theta = 40°$ case. Left: The *Unshaped* scheme shows coherent, structured error waves trailing the main pulse, indicative of dispersive phase lag. Right: The *Shaped* scheme suppresses these coherent errors, leaving only low-amplitude, unstructured noise, confirming high-fidelity advection.

3.3 2-D Isotropic Acoustic Propagation (Angle Sweep)

In Computational Aeroacoustics (CAA), preserving the isotropy of acoustic waves within a convective flow is paramount. Standard dimension-by-dimension reconstruction methods often introduce direction-dependent errors, where numerical dispersion and dissipation are minimized along grid axes $(0°, 90°)$ but deteriorate significantly in diagonal directions. To quantify these *directional isotropy errors*, we evaluate the propagation of small-amplitude acoustic pulses across a full range of propagation angles.

The background flow is uniform with a Mach number $M_\infty = 0.2$ aligned with the x-axis ($u_\infty = 0.2c_\infty$, $v_\infty = 0$). The propagation angle θ is swept from 0° to 180° by choosing integer wavenumber pairs (m_x, m_y) such that the radial wavenumber magnitude remains approximately constant at a target resolution of PPW ≈ 8 ($|\mathbf{k}_0|\Delta x \approx \pi/4$). The initial condition is a Gaussian-modulated acoustic perturbation with a small amplitude $A = 3 \times 10^{-6}$, ensuring the flow remains in the linear regime.

We analyze both acoustic branches, $s = +1$ (downstream/fast mode) and $s = -1$ (upstream/slow mode). The exact convective phase speed for these modes includes the

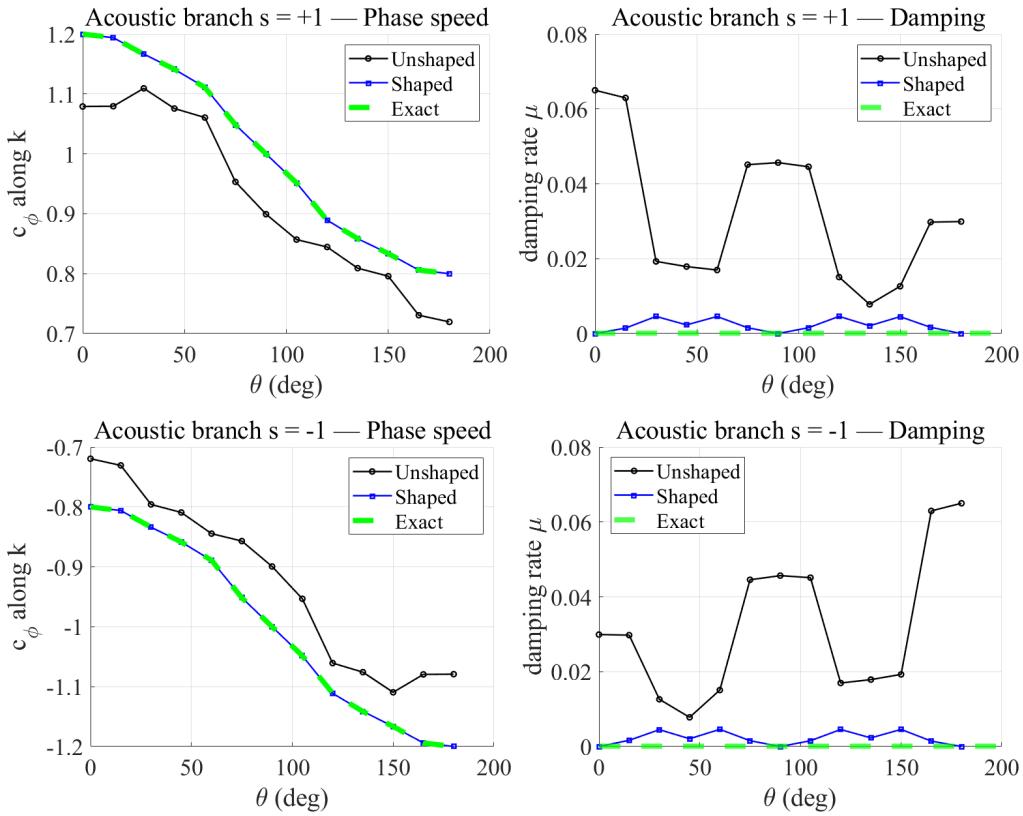

Figure 3.4: Angular sweep of dispersion and dissipation errors for acoustic waves at PPW=8. *Method:* CD2 reconstruction with Roe flux. Left column: Phase speed c_ϕ versus propagation angle θ. The dashed green line represents the exact Doppler-shifted physics. Right column: Damping rate μ versus θ. Top row: $s = +1$ branch (downstream propagating). Bottom row: $s = -1$ branch (upstream propagating).

Doppler shift effect:

$$c_{\phi,\text{exact}}(\theta, s) = \frac{k_x u_\infty + k_y v_\infty}{|\mathbf{k}_0|} + s\, c_\infty = U_\infty \cos\theta + s\, c_\infty. \tag{3.5}$$

Numerical diagnostics are performed using a moving window probe that tracks the theoretical group velocity of the packet. The numerical phase speed and damping rate are extracted from the complex modal amplitude $a(t; \mathbf{k}_0)$ via:

$$c_{\phi,\text{num}} = \frac{1}{|\mathbf{k}_0|}\frac{d}{dt}\arg a(t), \qquad \mu = -\frac{d}{dt}\ln|a(t)|. \tag{3.6}$$

Figure 3.4 illustrates a significant performance disparity between the baseline and

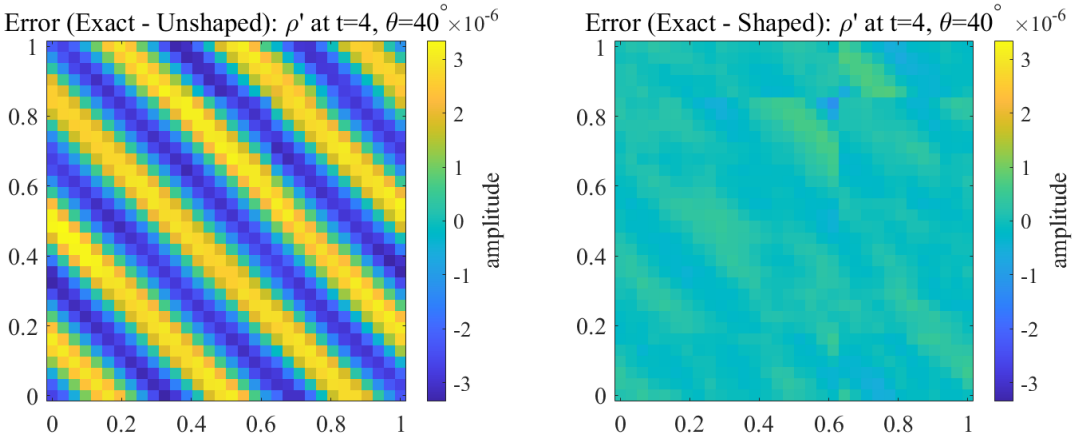

Figure 3.5: Spatial error distribution of the acoustic density perturbation ($\rho_{\text{exact}} - \rho_{\text{num}}$) at $t = 4.0$ for an oblique propagation angle of $\theta = 40°$ (PPW=8). Left: The *Unshaped* scheme error is dominated by coherent phase-lag structures. Right: The *Shaped* scheme significantly reduces structured error, demonstrating improved phase fidelity.

shaped schemes. The *Unshaped* scheme exhibits severe *grid anisotropy*; the phase speed deviates markedly from the exact solution at oblique angles (around 45° and 135°), and the numerical damping fluctuates directionally. This anisotropy implies that a circular acoustic pulse would deform into a diamond-like shape over time. In contrast, the *Shaped* scheme accurately tracks the exact Doppler-shifted phase speed for both left- ($s = -1$) and right-running ($s = +1$) waves across all propagation angles. The phase speed curves are nearly indistinguishable from the exact solution, demonstrating excellent *isotropy*. Furthermore, the numerical damping for the shaped scheme remains negligible (near-zero) regardless of the angle, validating that the Zero Pass-Band Dissipation (ZPD) property holds effectively in multi-dimensional convective environments.

This spectral analysis is corroborated by the spatial error plots in Figure 3.5 for a representative oblique angle of $\theta = 40°$ at $t = 4.0$. The error field of the *Unshaped* solution displays coherent, concentric wave structures. These artifacts are directly attributable to *dispersive phase lag*, where the numerical wave travels slower than the physical wave, leaving a trailing error wake. Conversely, the *Shaped* solution shows a substantial reduction in these structured errors. The remaining error field is composed of low-amplitude, unstructured residual noise, confirming that the proposed shaping strategy significantly enhances the fidelity of aeroacoustic propagation by correcting linear dispersion errors isotropically.

3.4 1-D Sod Shock Tube

We simulate the Sod shock tube problem to rigorously assess the scheme's shock-capturing accuracy, nonlinear robustness, and conservation properties. The domain is initialized with a discontinuity at $x_0 = 0.5$ separating two constant states:

$$(\rho, u, p)_L = (1.0, 0, 1.0), \qquad (\rho, u, p)_R = (0.125, 0, 0.1). \tag{3.7}$$

The exact solution comprises a left-going rarefaction wave, a contact discontinuity, and a right-going shock wave.

For this benchmark, we employ two baseline flux formulations: (i) Roe flux-difference splitting and (ii) AUSM$^+$-up. To ensure non-oscillatory behavior near discontinuities, a hybrid sensor based on pressure jump and Entropy-Shock Wave (ESW) detection is used to locally deactivate the spectral shaping and revert to the baseline dissipative scheme.

To verify that the proposed flux blending preserves the correct shock physics, we quantify the conservation errors using the Rankine-Hugoniot (RH) relations. The discrete residual $\mathcal{R}_{\text{RH}}$ is computed across the moving shock by extracting the states $\mathbf{U}_L, \mathbf{U}_R$ and fluxes $\mathbf{F}_L, \mathbf{F}_R$ from a window surrounding the maximum pressure gradient. The shock speed V_s is estimated from the continuity equation, and the residual is defined as:

$$\mathcal{R}_{\text{RH}} = \|(\mathbf{F}_R - \mathbf{F}_L) - V_s(\mathbf{U}_R - \mathbf{U}_L)\|_2. \tag{3.8}$$

Additionally, we measure the entropy jump Δs across the shock to ensure the solution satisfies the second law of thermodynamics (physical admissibility). The entropy is defined as $s = \ln(p/\rho^\gamma)$, and the jump is calculated as $\Delta s = s_R - s_L$.

Figures 3.6 and 3.7 present the comprehensive results for the Roe and AUSM+up schemes, respectively. As seen in the field plots (a) and zoomed views (b), the *Shaped* scheme (blue dashed line) significantly sharpens the contact discontinuity compared to the *Unshaped* baseline (black solid line) while maintaining a capture of the shock wave that is free of oscillations.

The diagnostic plots (c) confirm that the conservation errors remain negligible.

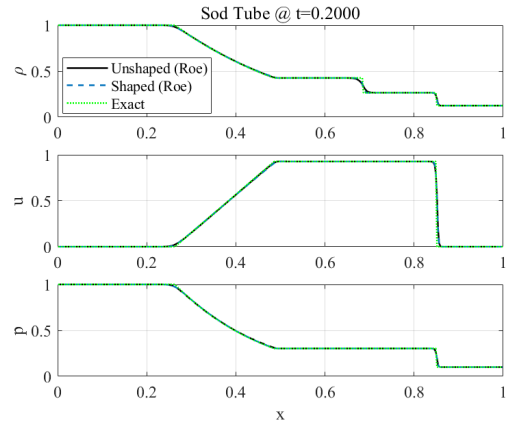

(a) Global Profiles

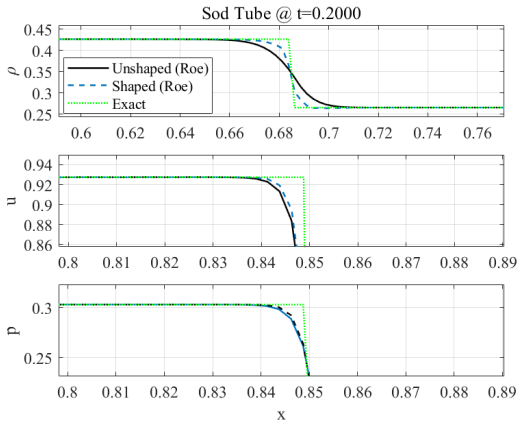

(b) Zoomed View

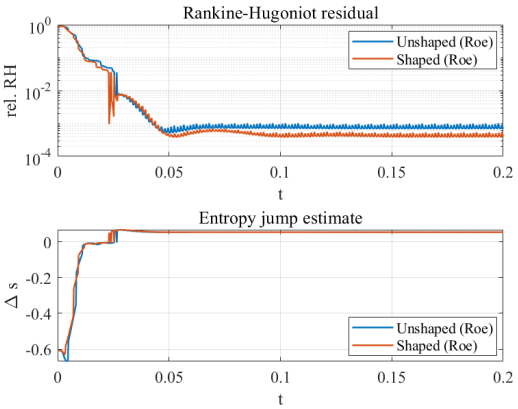

(c) Conservation Diagnostics

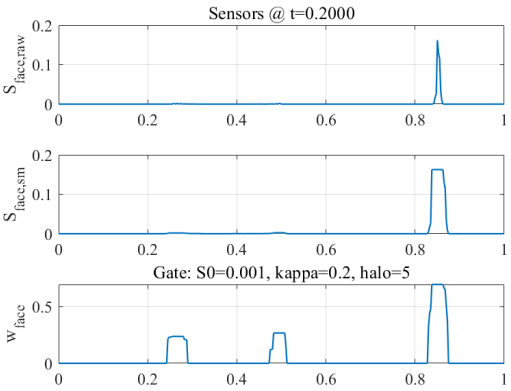

(d) Sensor Activation

Figure 3.6: Results for Roe Flux ($t = 0.20$). (a) Density, velocity, and pressure profiles. (b) Zoom-in on the contact discontinuity and shock. (c) History of RH residual and entropy jump estimate. (d) Sensor values detecting the shock and contact surfaces.

The RH residual for the *Shaped* scheme decays rapidly and remains bounded at low levels comparable to the baseline, indicating that the shaped flux maintains proper conservation properties. Furthermore, the computed entropy jump across the shock correctly matches the theoretical value of $\Delta s \approx 0.054$. The sensor activation plots (d) reveal a key feature of the method: the weighting function w_{face} activates ($w \to 1$) strongly at the shock ($x \approx 0.85$) to ensure stability, but remains inactive ($w \approx 0$) at the contact discontinuity ($x \approx 0.68$). This selective activation allows the spectral shaping to remain fully operational across the contact surface, directly leading to the observed reduction in numerical dissipation and the sharpening of the discontinuity profile.

It is worth noting that for the AUSM+up cases, we employ a “centralized” formula-

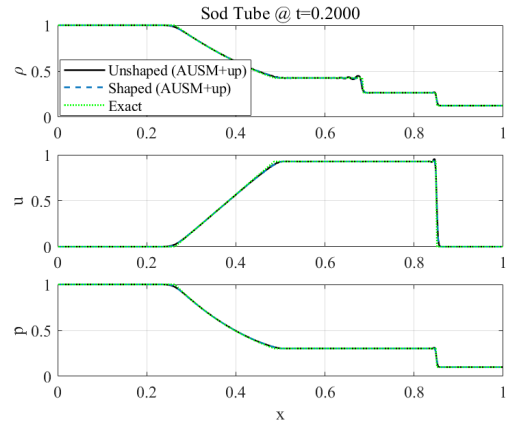

(a) Global Profiles

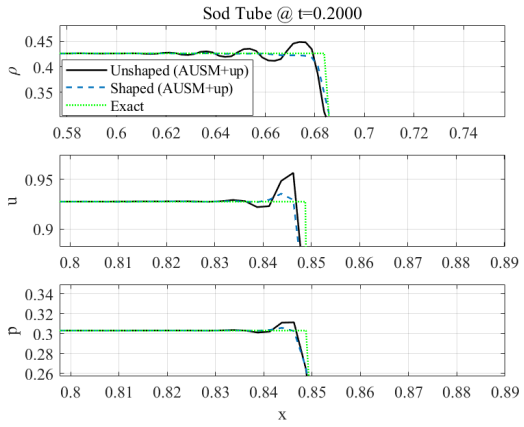

(b) Zoomed View

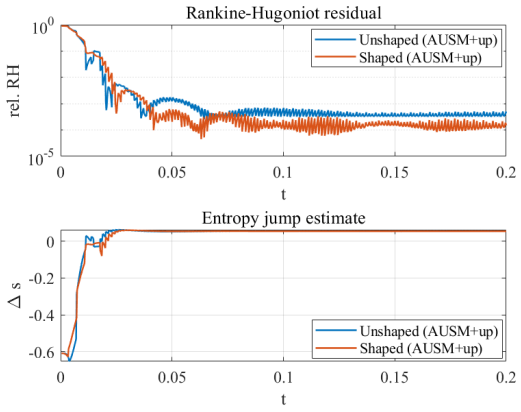

(c) Conservation Diagnostics

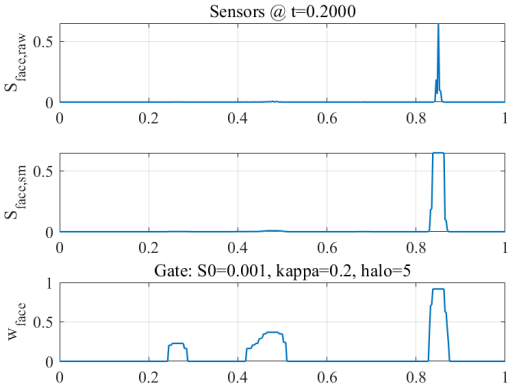

(d) Sensor Activation

Figure 3.7: Results for AUSM+up Flux ($t = 0.20$). Layout is identical to Figure 3.6.

tion for the advective flux in the transport path to maximize spectral resolution. While this strategy significantly reduces dissipation, it inherently introduces dispersive oscillations near discontinuities, as visible in the unshaped baseline results (solid black lines in Figure 3.7). However, the proposed sensor-based gating mechanism effectively mitigates these artifacts. By detecting the shock location ($x \approx 0.85$) and locally reverting to the robust upwind baseline (as shown in the sensor activation plot), the *Shaped* scheme successfully suppresses harmful oscillations while preserving the sharp resolution of the contact discontinuity.

Quantitatively, the L_1 density error norms listed in Table 3.3 demonstrate a clear accuracy gain. The *Shaped* scheme reduces the global error by approximately 22% for AUSM+up and 31% for Roe compared to their respective baselines. This improvement

Table 3.3: Comparison of L_1 density error norms for the Sod problem at $t = 0.20$.

Flux Scheme	***Unshaped*** L_1 **Error**	***Shaped*** L_1 **Error**	**Reduction (%)**
AUSM+up	2.343×10^{-3}	1.840×10^{-3}	21.5%
Roe	2.303×10^{-3}	1.584×10^{-3}	31.2%

is primarily driven by the reduced numerical dissipation at the contact discontinuity, which is a linearly degenerate wave that typically suffers from excessive smearing in standard upwind schemes.

3.5 Shu–Osher Shock–Entropy Interaction

We solve the Shu-Osher problem to evaluate the scheme's ability to capture strong shocks while resolving high-frequency post-shock entropy fluctuations. This problem serves as a critical proxy for shock-turbulence interaction in aeroacoustics. The specific problem configuration is adopted from Taylor et al. [47]. The domain is normalized to $x \in [0, 1]$. The initial condition consists of a moving Mach 3 shock located at $x_s = 0.125$, separating a post-shock state (L) from a pre-shock state (R) containing sinusoidal density fluctuations:

$$(\rho, u, p)_L = (3.857,\ 2.629,\ 10.333), \qquad (\rho, u, p)_R = (1 + 0.2\sin(16\pi(x - x_s)),\ 0,\ 1). \tag{3.9}$$

The simulation is performed on a fixed grid of $N = 1024$ cells and compared against a converged reference solution computed with $N_{\text{ref}} = 4096$.

The left boundary ($x = 0$) is specified as a Dirichlet condition fixed at the post-shock state $\mathbf{U}_L$. Since the flow velocity $u_L \approx 2.63$ is supersonic relative to the local sound speed ($a_L \approx 1.94$), all characteristic waves enter the domain from the left. This classifies the boundary as a supersonic inflow, for which prescribing all primitive variables is mathematically well-posed and physically consistent. The right boundary ($x = 1$) is maintained at the mean pre-shock state $\mathbf{U}_{R,\text{mean}} = (1, 0, 1)$. The simulation time is restricted to $t = 0.1775$ (< 0.21) to ensure that neither the primary shock nor the acoustic waves generated by the interaction reach the right boundary. Under this causality constraint, the right boundary acts as a far-field condition, and the fixed

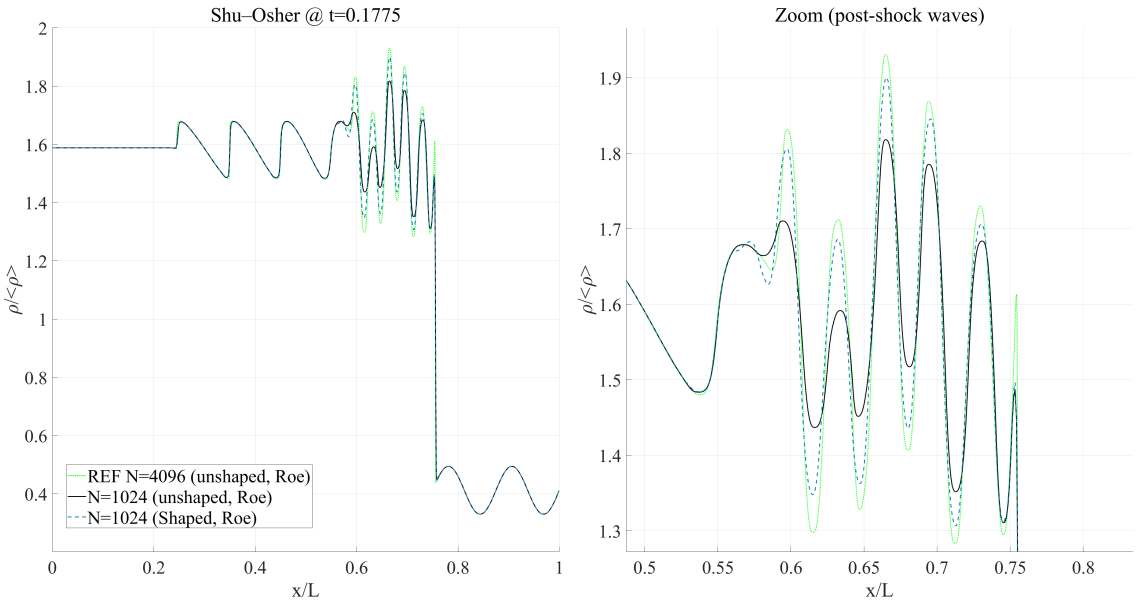

(a) Global Profiles

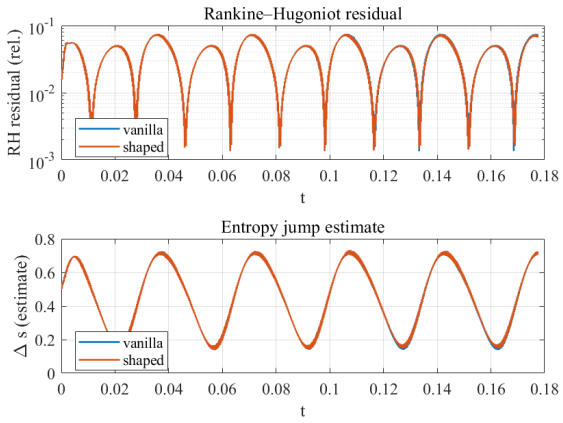

(b) Conservation Diagnostics

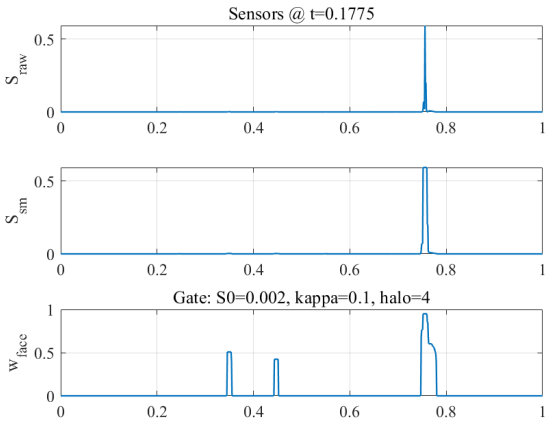

(c) Sensor Activation

Figure 3.8: Results for Roe Flux ($t = 0.1775, N = 1024$). (a) Density profiles showing the shock and entropy waves. (b) Zoomed view of the post-shock oscillations. (c) Rankine-Hugoniot residual and entropy jump. (d) Sensor activation map.

Dirichlet specification remains valid.

Figures 3.8 and 3.9 present the results for the Roe and AUSM+up schemes, respectively. The zoomed views (b) clearly demonstrate the advantage of the spectral flux shaping. The *Unshaped* schemes (black solid lines) suffer from significant amplitude decay and phase lag in the high-frequency entropy waves ($x \in [0.5, 0.8]$) due to excessive numerical dissipation. In contrast, the *Shaped* schemes (blue dashed lines) preserve the wave amplitudes and peak locations much more accurately, closely matching the

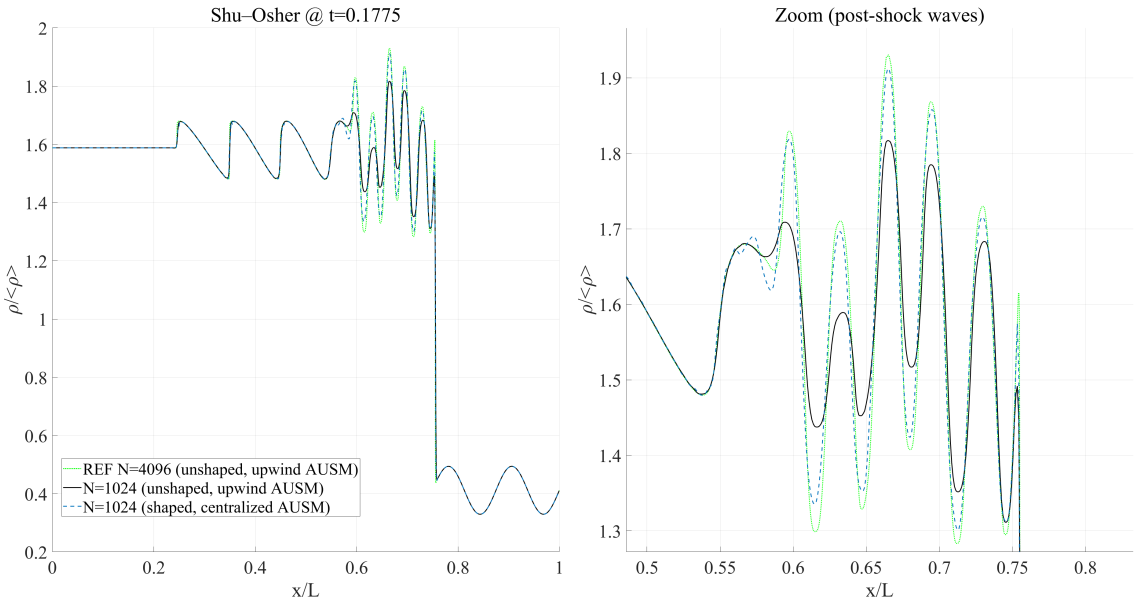

(a) Global Profiles

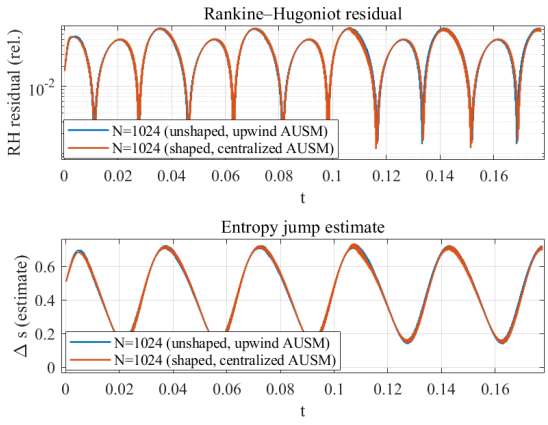

(b) Conservation Diagnostics

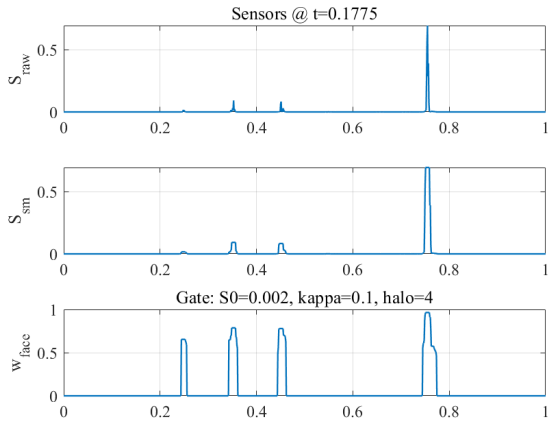

(c) Sensor Activation

Figure 3.9: Results for AUSM+up Flux ($t = 0.1775, N = 1024$). Layout is identical to Figure 3.8.

reference solution (green dotted line).

The conservation diagnostics (c) confirm that the shaped scheme maintains shock stability. The RH residuals oscillate due to the interaction with density waves but remain bounded and comparable to the baseline, indicating that the blending of shaped fluxes does not degrade the shock speed or strength calculation.

The quantitative performance is summarized in Table 3.4. The *Shaped* scheme delivers a dramatic reduction in L_1 error: approximately 51.6% for AUSM+up and

Table 3.4: Comparison of L_1 density error norms for the Shu-Osher problem ($N = 1024$). Errors are computed in the post-shock window $x \in [0.15, 0.95]$ against a reference solution ($N_{\text{ref}} = 4096$).

Flux Scheme	***Unshaped*** L_1 **Error**	***Shaped*** L_1 **Error**	**Reduction (%)**
AUSM+up	3.750×10^{-2}	1.814×10^{-2}	**51.6%**
Roe	3.845×10^{-2}	2.044×10^{-2}	**46.8%**

46.8% for Roe. This result highlights that the proposed method effectively minimizes dissipation in smooth, oscillatory regions (via the ZPD property) while robustly handling strong shocks via the sensor mechanism, making it highly suitable for direct numerical simulations of compressible turbulence and aeroacoustics.

3.6 Propagation of Acoustic, Entropy, and Vorticity Pulses

To rigorously evaluate the high-fidelity propagation characteristics of the proposed scheme, we simulate the simultaneous convection of acoustic, entropy, and vorticity pulses in a uniform mean flow. This problem is a standard benchmark in Computational Aeroacoustics for assessing a solver's ability to resolve these multi-modal waves simultaneously, testing both the nondispersive propagation of acoustic waves and the low-dissipation advection of flow disturbances.

The physical setup consists of a superposition of three initial perturbations in a uniform mean flow with Mach number $M_\infty = 0.5$ ($u_0 = 0.5, v_0 = 0$) on a 2D Cartesian grid. Specifically, an acoustic pulse is initialized at the origin $(0, 0)$, expanding radially while convecting downstream. This is accompanied by entropy and vorticity pulses, both centered at $(67, 0)$, which convect passively with the mean flow.

To rigorously isolate dispersive and dissipative errors from boundary artifacts, we employ an extended computational domain of 1200×1200 cells with $\Delta x = \Delta y = 1$. Since residual numerical reflections can persist over long integration times despite radiation boundary conditions [3], we perform computations on the large domain but analyze results within a zoomed window of $[-100, 100] \times [-100, 100]$ to ensure the region of interest remains reflection-free.

The solver utilizes the AUSM$^+$-up flux with MUSCL2 reconstruction. The spectral flux shaping (SFS) is applied using compact Padé filters optimized for zero pass-band

dissipation (ZPD) to preserve the amplitude of the high-frequency components.

We compare the *Shaped* scheme against the analytical exact solution provided in the original benchmark, derived using Bessel functions. The comparison is conducted at three distinct time instances: $t = 28.5$, $t = 57.0$, and $t = 80.0$, representing early, intermediate, and late stages of propagation. Since the vorticity pulse convects identically to the entropy pulse in this linear regime, the analysis focuses on density and pressure perturbations to validate the transport of entropy and acoustic modes, respectively.

Figure 3.10 illustrates the evolution of the density perturbation. Density carries information for both the acoustic pulse (expanding circles) and the entropy pulse (convecting Gaussian spot). At $t = 28.5$, the acoustic wavefront separates from the entropy pulse. By $t = 57.0$, the entropy pulse advects to $x \approx 95.5$, remaining within the analysis window. At $t = 80.0$, it reaches $x \approx 107$, mostly exiting the zoomed window ($x \in [-100, 100]$), which allows us to focus on the long-term quality of the acoustic wavefront and the absence of trailing dispersive wakes.

The contour plots show that the *Shaped* scheme maintains the circular isotropy of the acoustic wave without grid-induced deformation. More critically, the centerline cut plots (right column of Figure 3.10) demonstrate excellent agreement with the exact solution. The scheme successfully preserves the peak amplitude of the entropy pulse at $t = 57.0$, a regime where standard second-order schemes typically suffer from severe numerical diffusion.

Figure 3.11 presents the pressure perturbation fields. Unlike density, pressure is affected only by the acoustic pulse in this problem setup. The pulse originates at $(0, 0)$ and convects downstream due to the mean flow ($M = 0.5$), resulting in a Doppler-shifted expansion where the wavefront moves faster downstream than upstream. The centerline comparisons confirm that the *Shaped* scheme accurately captures the phase and amplitude of the acoustic pulse. Even at $t = 80.0$, where cumulative dispersion errors typically manifest as phase lag or lead, the numerical solution remains synchronized with the analytical solution. This indicates that the optimized dispersion relation of the shaped flux effectively minimizes phase errors over long-distance propagation.

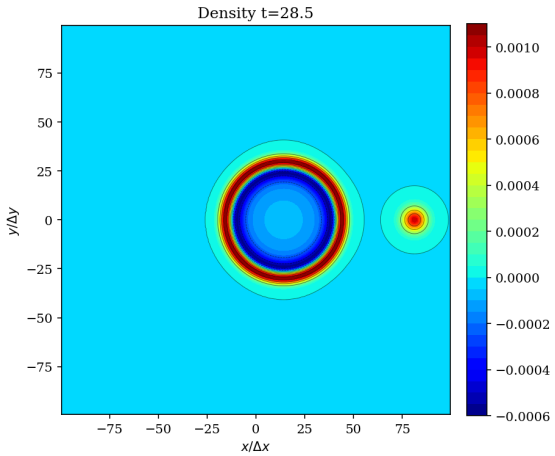

(a) Field at $t = 28.5$

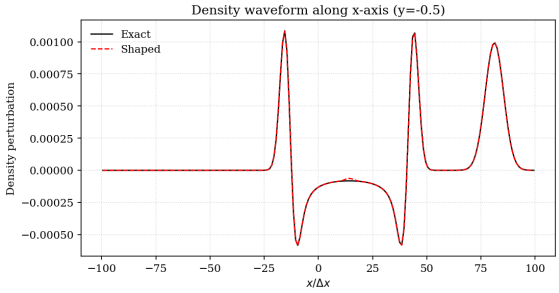

(b) Centerline at $t = 28.5$

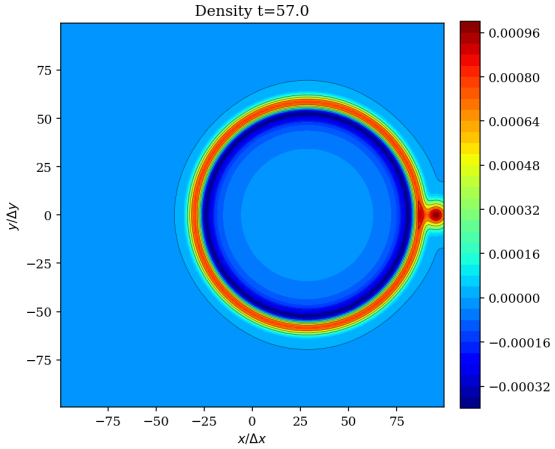

(c) Field at $t = 57.0$

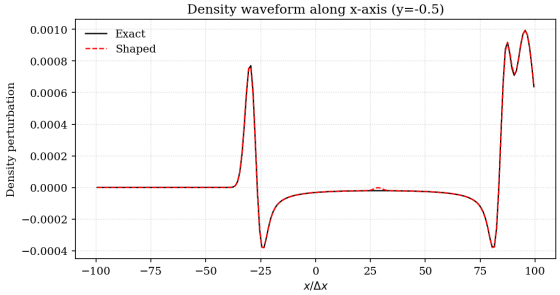

(d) Centerline at $t = 57.0$

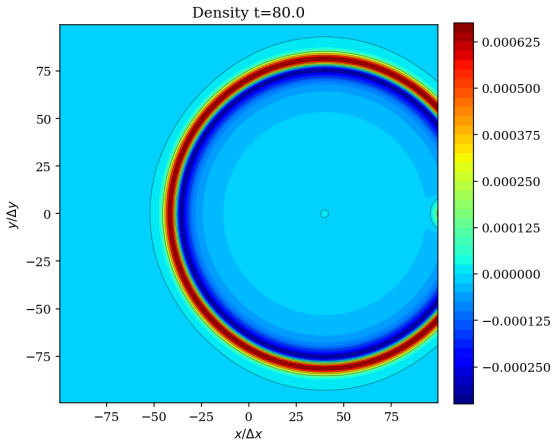

(e) Field at $t = 80.0$

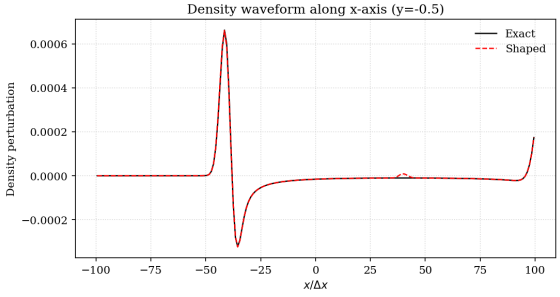

(f) Centerline at $t = 80.0$

Figure 3.10: Evolution of Density Perturbation. Left column: 2D contours of the numerical solution. Right column: Comparison of the centerline ($y = 0$) waveform between the Exact solution (black solid) and the Shaped scheme (red dashed). The entropy pulse (strong central peak) is well-resolved at $t = 28.5$ and $t = 57.0$, before leaving the window at $t = 80.0$.

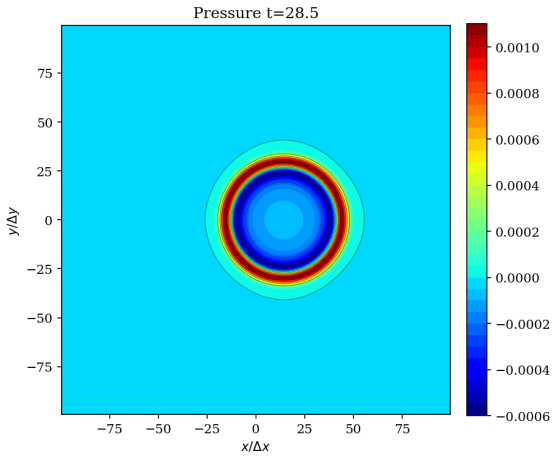

(a) Field at $t = 28.5$

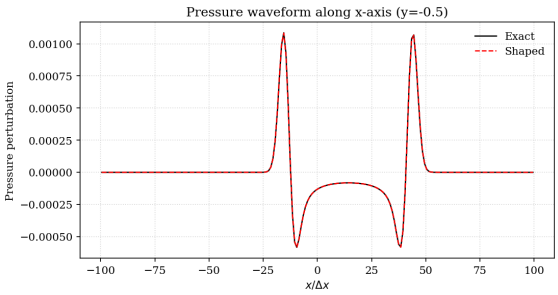

(b) Centerline at $t = 28.5$

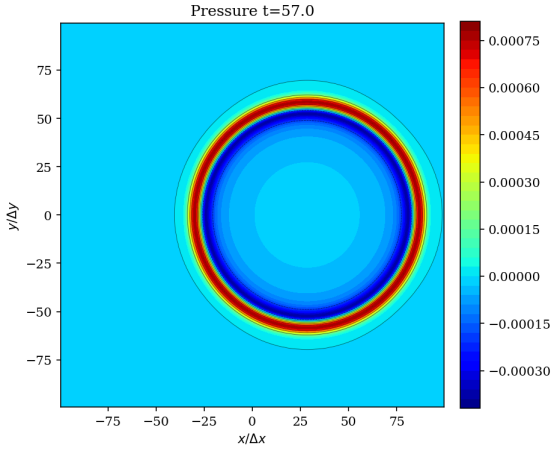

(c) Field at $t = 57.0$

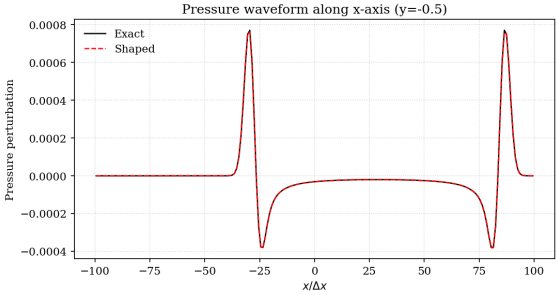

(d) Centerline at $t = 57.0$

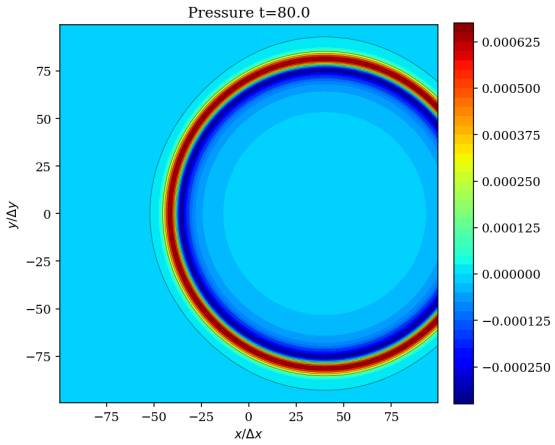

(e) Field at $t = 80.0$

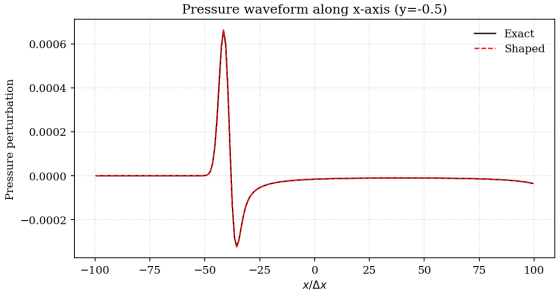

(f) Centerline at $t = 80.0$

Figure 3.11: Evolution of Pressure Perturbation. Left column: 2D contours. Right column: Centerline ($y = 0$) waveforms. The acoustic pulse exhibits correct Doppler-shifted convection, and the numerical solution captures the full amplitude without visible dispersive ripples.

Chapter 4

Conclusion

In this work, we have developed and validated the Spectral Flux-Shaping Finite-Volume Method (SFS-FVM), a novel framework designed to embed Dispersion-Relation-Preserving (DRP) principles within robust, conservative finite-volume solvers. The core of this approach is the separation of the numerical flux into distinct transport and diffusive paths, which are then shaped independently using efficient compact operators. This strategy allows for the explicit cancellation of dispersion errors on the transport path via a bounded Padé gain, while dissipation is precisely controlled on the diffusive path using a monotone spectral bump.

For upwind schemes such as Roe and AUSM+up, this framework enables a Zero Pass-Band Dissipation (ZPD) design, which completely eliminates numerical damping for well-resolved acoustic waves in smooth regions of the flow. To ensure robustness, a sensor-based gating mechanism smoothly transitions the scheme to its baseline shock-capturing formulation in the presence of discontinuities. A notable advantage of this strategy is that, at shocks, the method recovers the intrinsic physics-based stability of the approximate Riemann solver, avoiding the reliance on ad-hoc artificial viscosity coefficients often required by central difference schemes.

Numerical experiments have confirmed the dual capabilities of the proposed method. For delicate acoustic and convective wave propagation, the shaped schemes demonstrate superior fidelity, preserving wave energy and ensuring angular isotropy. The transport shaper effectively cancels dispersion errors, while the diffusion shaper enforcing ZPD leads to a dramatic reduction in amplitude decay, even at coarse resolutions. Furthermore, in challenging shock-capturing tests such as the Shu-Osher problem, the method remains fully robust and non-oscillatory. The schemes reproduce shock positions and stability on par with the baseline solvers while successfully resolving fine-scale post-shock entropy structures that are typically smeared by standard upwind methods, achieving an error reduction of approximately 50%. Finally, the pulse propagation benchmark confirmed

that the method maintains the isotropy of acoustic waves and preserves the amplitude of entropy pulses over long integration times, effectively mitigating the dispersive wake artifacts common in low-order schemes.

Overall, these results affirm that SFS-FVM integrates naturally with standard finite-volume solvers to provide shock-capturing reliability alongside wave-propagation fidelity. The proposed framework successfully unifies high-order accuracy for smooth waves with full robustness for discontinuities within a single, conservative context. Future work will focus on extending the proposed formulation to non-uniform or stretched grids, enabling the method to handle practical engineering geometries with varying resolution requirements.

Appendix A

Unified Linearized Analysis and Solver Details

This appendix provides the mathematical foundation for the schemes used in this study. It presents the linearized von Neumann analysis used to quantify dispersion and dissipation errors, explicitly deriving the spectral properties of the baseline MUSCL3 scheme from first principles, and summarizes implementation details for the Roe and AUSM+up solvers.

A.1 Baseline Spatial Discretization: Analysis of MUSCL3 and Standard Schemes

To demonstrate the spectral characteristics of high-order shock-capturing schemes, we utilize the third-order MUSCL reconstruction (QUICK) coupled with a Rusanov (local Lax–Friedrichs) numerical flux as a representative baseline case. While numerous spatial reconstruction methods exist (e.g., CD2, CD4, MUSCL2), we select MUSCL3 ($\kappa = 1/3$) for this detailed derivation to illustrate the analysis framework [48].

A.1.1 Finite-volume form and Rusanov numerical flux (system form)

We consider a 1D conservation law

$$\partial_t \mathbf{U} + \partial_x \mathbf{F}(\mathbf{U}) = 0, \tag{A.1}$$

on a uniform grid with spacing h. Let $\bar{\mathbf{U}}_i$ denote the cell-average state in cell i. The semi-discrete finite-volume update is

$$\frac{d\bar{\mathbf{U}}_i}{dt} = -\frac{\widehat{\mathbf{F}}_{i+\frac{1}{2}} - \widehat{\mathbf{F}}_{i-\frac{1}{2}}}{h}. \tag{A.2}$$

The numerical flux at each interface is defined by the Rusanov (local Lax–Friedrichs) form

$$\widehat{\mathbf{F}}_{i+\frac{1}{2}} = \frac{1}{2}\Big(\mathbf{F}(\mathbf{U}^L_{i+\frac{1}{2}}) + \mathbf{F}(\mathbf{U}^R_{i+\frac{1}{2}})\Big) - \frac{1}{2}\,\lambda_{\max,i+\frac{1}{2}}\Big(\mathbf{U}^R_{i+\frac{1}{2}} - \mathbf{U}^L_{i+\frac{1}{2}}\Big), \tag{A.3}$$

where $\lambda_{\max,i+\frac{1}{2}}$ is a local maximum wave-speed estimate, e.g.

$$\lambda_{\max,i+\frac{1}{2}} = \max\Big(\rho(\mathbf{A}(\mathbf{U}^L_{i+\frac{1}{2}})),\ \rho(\mathbf{A}(\mathbf{U}^R_{i+\frac{1}{2}}))\Big), \qquad \mathbf{A}(\mathbf{U}) = \frac{\partial \mathbf{F}}{\partial \mathbf{U}}. \tag{A.4}$$

Equivalently, $\rho(\mathbf{A}) = \max_n |\lambda_n(\mathbf{A})|$ is the spectral radius. In this form, the dissipation operator is $\mathbf{D}_{i+\frac{1}{2}} = \lambda_{\max,i+\frac{1}{2}}\mathbf{I}$.

A.1.2 U-MUSCL reconstruction (componentwise vector form)

The interface states $\mathbf{U}^L_{i+\frac{1}{2}}$ and $\mathbf{U}^R_{i+\frac{1}{2}}$ are reconstructed from cell averages using the U-MUSCL scheme with parameter κ, applied componentwise. We first define the backward and forward differences at index i:

$$\Delta\mathbf{U}^-_i = \bar{\mathbf{U}}_i - \bar{\mathbf{U}}_{i-1}, \qquad \Delta\mathbf{U}^+_i = \bar{\mathbf{U}}_{i+1} - \bar{\mathbf{U}}_i. \tag{A.5}$$

The reconstructed states are given by:

$$\mathbf{U}^L_{i+\frac{1}{2}} = \bar{\mathbf{U}}_i + \frac{1}{4}\Big((1-\kappa)\Delta\mathbf{U}^-_i + (1+\kappa)\Delta\mathbf{U}^+_i\Big), \tag{A.6}$$

$$\mathbf{U}^R_{i+\frac{1}{2}} = \bar{\mathbf{U}}_{i+1} - \frac{1}{4}\Big((1-\kappa)\Delta\mathbf{U}^+_{i+1} + (1+\kappa)\Delta\mathbf{U}^-_{i+1}\Big). \tag{A.7}$$

Setting $\kappa = 1/3$ (MUSCL3) yields

$$\mathbf{U}^L_{i+\frac{1}{2}} = -\frac{1}{6}\bar{\mathbf{U}}_{i-1} + \frac{5}{6}\bar{\mathbf{U}}_i + \frac{1}{3}\bar{\mathbf{U}}_{i+1}, \tag{A.8}$$

$$\mathbf{U}^R_{i+\frac{1}{2}} = \frac{1}{3}\bar{\mathbf{U}}_i + \frac{5}{6}\bar{\mathbf{U}}_{i+1} - \frac{1}{6}\bar{\mathbf{U}}_{i+2}. \tag{A.9}$$

Similarly, at $i - \frac{1}{2}$,

$$\mathbf{U}^L_{i-\frac{1}{2}} = -\frac{1}{6}\bar{\mathbf{U}}_{i-2} + \frac{5}{6}\bar{\mathbf{U}}_{i-1} + \frac{1}{3}\bar{\mathbf{U}}_i, \qquad \mathbf{U}^R_{i-\frac{1}{2}} = \frac{1}{3}\bar{\mathbf{U}}_{i-1} + \frac{5}{6}\bar{\mathbf{U}}_i - \frac{1}{6}\bar{\mathbf{U}}_{i+1}. \tag{A.10}$$

A.1.3 Von Neumann Analysis (semi-discrete 1D FV wave analysis)

Substituting the MUSCL3 interface states into the FV update (A.2) and using the linear-advection Rusanov flux, for $c > 0$ we have $\widehat{\mathbf{F}}_{i+\frac{1}{2}} = c\,\mathbf{U}^L_{i+\frac{1}{2}}$. Hence the semi-discrete scheme becomes

$$\frac{d\bar{\mathbf{U}}_i}{dt} + \frac{c}{h}\left(\frac{1}{3}\bar{\mathbf{U}}_{i+1} + \frac{1}{2}\bar{\mathbf{U}}_i - \bar{\mathbf{U}}_{i-1} + \frac{1}{6}\bar{\mathbf{U}}_{i-2}\right) = \mathbf{0}. \tag{A.11}$$

To analyze dispersion and dissipation, we assume a plane-wave ansatz

$$\bar{\mathbf{U}}(x,t) = \tilde{\mathbf{U}}\, e^{\mathrm{i}(\omega t - kx)}. \tag{A.12}$$

Strictly, for FV methods the cell average is

$$\bar{\mathbf{U}}_i(t) = \frac{1}{h}\int_{x_i-\frac{h}{2}}^{x_i+\frac{h}{2}} \tilde{\mathbf{U}}\, e^{\mathrm{i}(\omega t - kx)}\, dx = \tilde{\mathbf{U}}\, e^{\mathrm{i}(\omega t - kx_i)}\left(\frac{\sin(kh/2)}{kh/2}\right), \tag{A.13}$$

but the sinc factor multiplies every linear term equally and thus cancels in the von Neumann substitution. Therefore we use the standard discrete relation

$$\bar{\mathbf{U}}_{i+m} = \bar{\mathbf{U}}_i\, e^{-\mathrm{i}m\theta}, \qquad \theta \equiv kh, \qquad m \in \mathbb{Z}, \tag{A.14}$$

where the negative sign follows from the phase $\omega t - kx$.

Substituting into (A.11) yields

$$\mathrm{i}\omega + \frac{c}{h}\left(\frac{1}{3}e^{-\mathrm{i}\theta} + \frac{1}{2} - e^{\mathrm{i}\theta} + \frac{1}{6}e^{2\mathrm{i}\theta}\right) = 0. \tag{A.15}$$

Using $e^{\mathrm{i}\theta} = \cos\theta + \mathrm{i}\sin\theta$, we obtain

$$\mathrm{i}\omega + \frac{c}{h}\Big[\underbrace{\left(\frac{1}{2} - \frac{2}{3}\cos\theta + \frac{1}{6}\cos 2\theta\right)}_{\text{diffusive}} + \mathrm{i}\underbrace{\left(-\frac{4}{3}\sin\theta + \frac{1}{6}\sin 2\theta\right)}_{\text{transport}}\Big] = 0. \tag{A.16}$$

Setting $c = 1$ for convenience, the dispersion and dissipation follow from ω.

Real part (dispersion). From (A.16),

$$\Re(\omega) = \frac{1}{h}\left(\frac{4}{3}\sin\theta - \frac{1}{6}\sin 2\theta\right). \tag{A.17}$$

Thus the numerical phase and group speeds are

$$v_p = \frac{\Re(\omega)}{k} = \frac{1}{\theta}\left(\frac{4}{3}\sin\theta - \frac{1}{6}\sin 2\theta\right), \qquad v_g = \frac{d\,\Re(\omega)}{dk} = \frac{d\,\Re(\omega)}{d\theta}\,h = \frac{4}{3}\cos\theta - \frac{1}{3}\cos 2\theta. \tag{A.18}$$

Imaginary part (dissipation). The numerical dissipation rate is

$$\Im(\omega) = \frac{1}{h}\left(\frac{1}{2} - \frac{2}{3}\cos\theta + \frac{1}{6}\cos 2\theta\right) \geq 0, \tag{A.19}$$

indicating diffusive behavior for all $\theta > 0$.

A.1.4 Extension to the Linearized Euler Equations (LEE)

We extend the scalar analysis to a linear hyperbolic *system* by considering the 1D linearized Euler equations about a constant base state $\mathbf{U}_0$:

$$\partial_t \mathbf{U}' + \mathbf{A}_0 \, \partial_x \mathbf{U}' = 0, \qquad \mathbf{A}_0 \equiv \left. \frac{\partial \mathbf{F}}{\partial \mathbf{U}} \right|_{\mathbf{U}_0}. \tag{A.20}$$

On a uniform grid, the semi-discrete finite-volume update with a central-plus-dissipation numerical flux is given by:

$$\frac{d\bar{\mathbf{U}}_i}{dt} = -\frac{1}{h} \left(\widehat{\mathbf{F}}_{i+\frac{1}{2}} - \widehat{\mathbf{F}}_{i-\frac{1}{2}} \right), \tag{A.21}$$

where

$$\widehat{\mathbf{F}}_{i+\frac{1}{2}} = \frac{1}{2}\Big(\mathbf{F}(\mathbf{U}^L_{i+\frac{1}{2}}) + \mathbf{F}(\mathbf{U}^R_{i+\frac{1}{2}}) \Big) - \frac{1}{2} \, \mathbf{D}_{i+\frac{1}{2}} \Big(\mathbf{U}^R_{i+\frac{1}{2}} - \mathbf{U}^L_{i+\frac{1}{2}} \Big). \tag{A.22}$$

For the baseline schemes considered, the dissipative operator is $\mathbf{D} = \lambda_{\max}\mathbf{I}$ (KT/Rusanov) or $\mathbf{D} = |\mathbf{A}_0|$ (Roe).

Matrix symbol and decoupling. Substituting a discrete Fourier mode $\bar{\mathbf{U}}_i(t) = \widehat{\mathbf{U}}(t)\, e^{-\mathrm{i}\theta}$ into the update yields the semi-discrete evolution equation $d\widehat{\mathbf{U}}/dt = \mathcal{L}(\theta)\widehat{\mathbf{U}}$, with the matrix symbol:

$$\mathcal{L}(\theta) = \frac{1}{2h}\Big(\mathbf{A}_0 \, \Phi_A(\theta) - \mathbf{D} \, \Phi_D(\theta) \Big). \tag{A.23}$$

Here, $\Phi_A(\theta)$ and $\Phi_D(\theta)$ are the scalar transport and diffusion symbols defined previously. The complex angular frequencies ω_n are related to the eigenvalues of this operator by $\omega_n(\theta) = -\mathrm{i}\,\mathrm{eig}_n(\mathcal{L}(\theta))$.

When $\mathbf{D}$ commutes with $\mathbf{A}_0$ (as in the KT/Rusanov and Roe cases), the system can be diagonalized simultaneously. Using the eigendecomposition $\mathbf{A}_0 = \mathbf{R}\mathbf{\Lambda}\mathbf{R}^{-1}$, the

matrix symbol decouples into scalar relations for each characteristic mode n:

$$\omega_n(\theta) = \frac{\mathrm{i}}{2h}\Big(\lambda_n \Phi_A(\theta) - d(\lambda_n)\Phi_D(\theta)\Big), \tag{A.24}$$

where λ_n are the eigenvalues of $\mathbf{A}_0$, and $d(\lambda_n)$ are the eigenvalues of $\mathbf{D}$ (e.g., $d(\lambda_n) = \lambda_{\max}$ for Rusanov or $d(\lambda_n) = |\lambda_n|$ for Roe).

The dispersion and dissipation characteristics are then extracted from the real and imaginary parts of ω_n:

$$c_{\phi,n} = \frac{\Re(\omega_n)}{k}, \qquad c_{g,n} = h\,\frac{d\,\Re(\omega_n)}{d\theta}, \qquad \mu_n = \Im(\omega_n). \tag{A.25}$$

If $\mathbf{D}$ does not commute with $\mathbf{A}_0$ (e.g., standard AUSM+up), the eigenvalues of $\mathcal{L}(\theta)$ must be computed numerically from (A.23).

A.1.5 Spectral Characteristics of Other Standard Schemes

The analysis framework above is general. For completeness, we list the transport and diffusion symbols $\Phi_A(\theta)$ and $\Phi_D(\theta)$ for several standard reconstructions on a uniform grid, using the same semi-discrete symbol convention as in the main text:

$$\mathcal{L}(\theta) = \frac{\mathrm{i}}{2h}\Big(\mathbf{A}_0\,\Phi_A(\theta) - \mathbf{D}\,\Phi_D(\theta)\Big), \qquad \theta \equiv kh, \qquad \mathrm{i}\omega_n = \mathrm{eig}_n(\mathcal{L}(\theta)). \tag{A.26}$$

In particular, for purely central (non-diffusive) schemes, $\Phi_D(\theta) \equiv 0$ and the modified wavenumber $\alpha(\theta)$ used in the main text satisfies $\Phi_A(\theta) = 2\alpha(\theta)$ under (A.26).

Second-order central (CD2).

$$\Phi_A^{\mathrm{CD2}}(\theta) = 2\sin\theta, \qquad \Phi_D^{\mathrm{CD2}}(\theta) = 0. \tag{A.27}$$

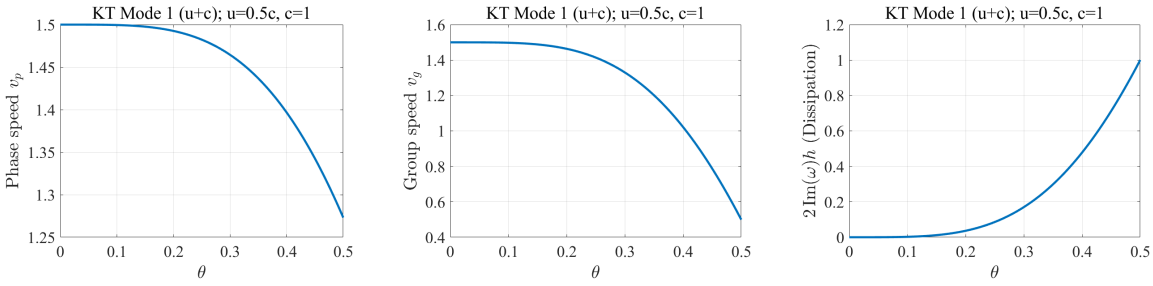

(a) Phase Velocity (v_p) (b) Group Velocity (v_g) (c) Dissipation (2Im(ω)h)

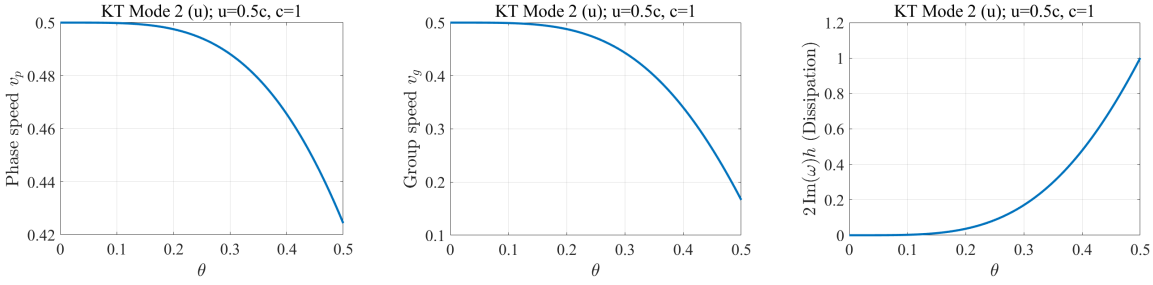

(d) Phase Velocity (v_p) (e) Group Velocity (v_g) (f) Dissipation (2Im(ω)h)

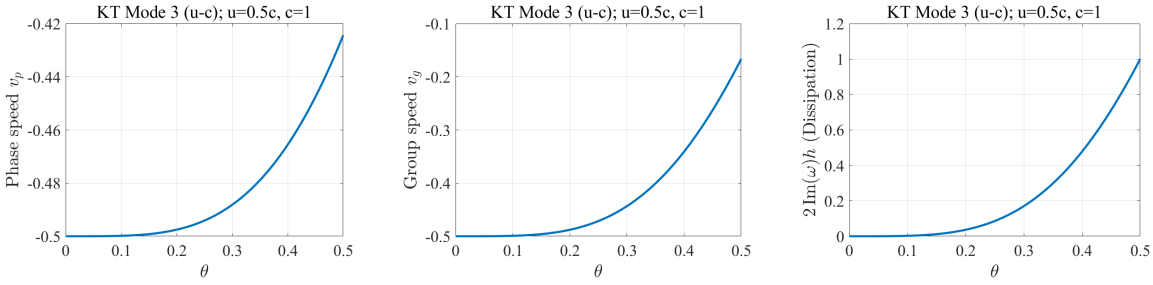

(g) Phase Velocity (v_p) (h) Group Velocity (v_g) (i) Dissipation (2Im(ω)h)

Figure A.1: Dispersion and dissipation characteristics of the baseline MUSCL3 scheme combined with the KT flux for linearized Euler equations ($M = 0.5$). Rows correspond to the three characteristic modes: Mode 1 ($u + c$), Mode 2 (u), and Mode 3 ($u - c$). Columns show normalized phase velocity, group velocity, and numerical dissipation, respectively.

Fourth-order central (CD4).

$$\Phi_A^{\mathrm{CD4}}(\theta) = \frac{1}{3}\Big(8\sin\theta - \sin(2\theta)\Big), \qquad \Phi_D^{\mathrm{CD4}}(\theta) = 0. \tag{A.28}$$

Second-order upwind (MUSCL2: Beam–Warming (BW)).

$$\Phi_A^{\mathrm{M2}}(\theta) = 2\sin\theta\,(2-\cos\theta), \qquad \Phi_D^{\mathrm{M2}}(\theta) = 4\sin^4\!\left(\frac{\theta}{2}\right). \tag{A.29}$$

Second-order upwind (MUSCL2: Fromm).

$$\Phi_A^{\mathrm{Fromm}}(\theta) = 3\sin\theta - \sin(2\theta), \qquad \Phi_D^{\mathrm{Fromm}}(\theta) = 2\sin^4\!\left(\frac{\theta}{2}\right). \tag{A.30}$$

Third-order upwind (MUSCL3: QUICK, $\kappa = \frac{1}{3}$).

$$\Phi_A^{\mathrm{QUICK}}(\theta) = \frac{1}{3}\Big(8\sin\theta - \sin(2\theta)\Big), \qquad \Phi_D^{\mathrm{QUICK}}(\theta) = \frac{4}{3}\sin^4\!\left(\frac{\theta}{2}\right). \tag{A.31}$$

A.2 Roe Scheme: Linearization and Implementation

The Roe scheme utilizes the eigenstructure of the Euler equations, enabling *matrix dissipation* in which numerical viscosity is scaled wave-by-wave in characteristic space.

A.2.1 Roe flux and Roe averages

The Roe flux at interface $i+\frac{1}{2}$ is

$$\widehat{\mathbf{F}}_{i+\frac{1}{2}} = \frac{1}{2}\Big(\mathbf{F}(\mathbf{U}^L_{i+\frac{1}{2}}) + \mathbf{F}(\mathbf{U}^R_{i+\frac{1}{2}})\Big) - \frac{1}{2}\,|\tilde{\mathbf{A}}_{i+\frac{1}{2}}|\,\Big(\mathbf{U}^R_{i+\frac{1}{2}} - \mathbf{U}^L_{i+\frac{1}{2}}\Big), \tag{A.32}$$

where $\tilde{\mathbf{A}}_{i+\frac{1}{2}}$ is the flux Jacobian evaluated at the Roe-averaged state. For the 1D Euler equations, the Roe averages can be expressed as

$$\tilde{u} = \frac{\sqrt{\rho_L}u_L + \sqrt{\rho_R}u_R}{\sqrt{\rho_L} + \sqrt{\rho_R}}, \qquad \tilde{H} = \frac{\sqrt{\rho_L}H_L + \sqrt{\rho_R}H_R}{\sqrt{\rho_L} + \sqrt{\rho_R}}, \qquad \tilde{a} = \sqrt{(\gamma-1)\Big(\tilde{H} - \tfrac{1}{2}\tilde{u}^2\Big)}. \tag{A.33}$$

The Roe matrix absolute value is defined through eigendecomposition

$$|\tilde{\mathbf{A}}| = \mathbf{R}\,|\mathbf{\Lambda}|\,\mathbf{R}^{-1}, \qquad |\mathbf{\Lambda}| = \mathrm{diag}\Big(|\tilde{\lambda}_1|, |\tilde{\lambda}_2|, |\tilde{\lambda}_3|\Big), \tag{A.34}$$

with eigenvalues $\tilde{\lambda}_{1,3} = \tilde{u} \pm \tilde{a}$ and $\tilde{\lambda}_2 = \tilde{u}$.

A.2.2 Dispersion and dissipation analysis (linearized symbol form)

For von Neumann analysis, we linearize about a uniform base state $\mathbf{U}_0$, so that $\mathbf{A}_0 = \partial\mathbf{F}/\partial\mathbf{U}|_{\mathbf{U}_0}$ is constant and

$$|\mathbf{A}_0| = \mathbf{R}\,|\mathbf{\Lambda}|\,\mathbf{R}^{-1}. \tag{A.35}$$

Because $\Phi_A(\theta)$ and $\Phi_D(\theta)$ are scalar symbols, they commute with matrices. Hence the semi-discrete operator decouples into characteristic modes and the matrix symbol takes the form

$$\mathcal{L}(\theta) = \frac{\mathrm{i}}{2h}\Big(\mathbf{A}_0\,\Phi_A(\theta) - |\mathbf{A}_0|\,\Phi_D(\theta)\Big), \qquad i\omega_n = \mathrm{eig}_n\Big(\mathcal{L}(\theta)\Big), \quad n = 1, 2, 3. \tag{A.36}$$

Equivalently, each characteristic mode satisfies the scalar dispersion relation

$$\omega_n(\theta) = \frac{\mathrm{i}}{2h}\Big(\lambda_n\,\Phi_A(\theta) - |\lambda_n|\,\Phi_D(\theta)\Big), \qquad n = 1, 2, 3, \tag{A.37}$$

where λ_n are the eigenvalues of $\mathbf{A}_0$. This makes explicit the low-Mach advantage of Roe dissipation: the entropy/contact mode scales with $|\lambda_2| = |u_0|$, while acoustic modes scale with $|u_0 \pm c|$.

A.2.3 Implementation details

To ensure robustness in nonlinear test cases, we apply two standard modifications.

Harten–Hyman entropy fix. To prevent nonphysical expansion shocks, the absolute value $|\lambda|$ is replaced by a smoothed function $|\lambda|_\varepsilon$ for eigenvalues near zero:

$$|\lambda|_\varepsilon = \begin{cases} \frac{1}{2}\left(\frac{\lambda^2}{\varepsilon} + \varepsilon\right), & |\lambda| < \varepsilon, \\ |\lambda|, & \text{otherwise}, \end{cases} \qquad \varepsilon = \kappa \max(0, \tilde{a} - \delta a), \qquad \kappa \in [0.05, 0.20]. \tag{A.38}$$

Local Lax–Friedrichs (LLF) blend. For additional robustness at very strong shocks, a small amount of LLF flux may be blended based on the shock sensor S:

$$\widehat{\mathbf{F}} \leftarrow (1-\eta)\widehat{\mathbf{F}}_{\text{Roe}} + \eta\,\widehat{\mathbf{F}}_{\text{LLF}}, \qquad \eta = \varepsilon_{\text{llf}}^{\text{base}} + \varepsilon_{\text{llf}}^{\text{shock}} S. \tag{A.39}$$

A.3 AUSM+up Scheme: Linearization and Implementation

The AUSM+up scheme treats convective and pressure contributions separately. In contrast to Roe-type solvers, its dissipation contribution is not generally expressible as a matrix absolute value $|\mathbf{A}|$ that shares eigenvectors with the flux Jacobian. Consequently, the linearized semi-discrete operator must be analyzed as a coupled system.

A.3.1 Flux split: Unshaped vs. centralized

Unshaped Formulation. The standard AUSM+up interface flux is constructed using split Mach numbers $\mathcal{M}^\pm$ and pressure polynomials $\mathcal{P}^\pm$:

$$\widehat{\mathbf{F}}_{i+\frac{1}{2}} = \dot{m}_{i+\frac{1}{2}} \boldsymbol{\psi}_{L/R} + p_{i+\frac{1}{2}} \mathbf{N}, \quad \mathbf{N} = [0, 1, 0]^\top, \tag{A.40}$$

where the mass flux is $\dot{m}_{i+\frac{1}{2}} = a_{i+\frac{1}{2}}(\rho_L \mathcal{M}_L^+ + \rho_R \mathcal{M}_R^-)$. The splitting polynomials for a given Mach number M are defined as:

$$\mathcal{M}^{\pm}(M) = \begin{cases} \frac{1}{2}(M \pm |M|), & |M| \geq 1, \\ \pm\frac{1}{4}(M \pm 1)^2 \pm \frac{1}{8}(M^2-1)^2, & |M| < 1. \end{cases} \tag{A.41}$$

The pressure splitting $\mathcal{P}^{\pm}$ typically uses a fifth-order polynomial for $|M| < 1$ to ensure C^1 continuity.

Centralized Formulation (for Shaping). For spectral shaping, we recast the same flux into a form that explicitly separates the dispersion-bearing central part from the diffusive upwind part. To ensure exact equivalence with the standard scheme ($\widehat{\mathbf{F}} = \widehat{\mathbf{F}}_{\text{AUSM}}$), the diffusive path must account for both the explicit stabilization terms (K_p, K_u) and the implicit dissipation arising from the Mach splitting:

$$\widehat{\mathbf{F}} = \underbrace{\widehat{\mathbf{F}}^{\text{adv}} + \widehat{\mathbf{F}}^{\text{press}}}_{\text{transport path (central)}} + \underbrace{\widehat{\mathbf{F}}^{\text{UP}}}_{\text{diffusive path (dissipation)}}. \tag{A.42}$$

The components are defined as:

$$\widehat{\mathbf{F}}^{\text{adv}} = \begin{bmatrix} \rho_f u_f \\ \rho_f u_f^2 \\ \rho_f u_f H_f \end{bmatrix}, \qquad \widehat{\mathbf{F}}^{\text{press}} = \begin{bmatrix} 0 \\ p_f \\ 0 \end{bmatrix}, \tag{A.43}$$

$$\widehat{\mathbf{F}}^{\text{UP}} = \dot{m}_{\text{diff}} \boldsymbol{\psi}^* + \begin{bmatrix} -K_p \, \phi \, \dfrac{\Delta p}{a_f} \\ -K_p \, \phi \, \dfrac{\Delta p}{a_f} \, u_f \; - \; K_u \, \phi \, \rho_f a_f \, \Delta u \\ -K_p \, \phi \, \dfrac{\Delta p}{a_f} \, H_f \end{bmatrix}, \tag{A.44}$$

where $\dot{m}_{\text{diff}} = \dot{m}_{i+\frac{1}{2}} - \rho_f u_f$ represents the mass-flux dissipation, and $\boldsymbol{\psi}^*$ is the upwind convected vector. (Note: In our implementation, this separation is efficiently achieved by computing the standard AUSM+up flux $\widehat{\mathbf{F}}_{\text{AUSM}}$ and the central flux $\widehat{\mathbf{F}}_{\text{central}}$ separately,

then defining the diffusive path as $\widehat{\mathbf{F}}^{\mathrm{UP}} = \widehat{\mathbf{F}}_{\mathrm{AUSM}} - \widehat{\mathbf{F}}_{\mathrm{central}}$).

A.3.2 Coupled linear analysis

Linearizing about a uniform base state $\mathbf{U}_0$ yields a constant flux Jacobian $\mathbf{A}_0 = \partial\mathbf{F}/\partial\mathbf{U}|_{\mathbf{U}_0}$. The linearized AUSM+up diffusive contribution can be written in the generic matrix form

$$\mathbf{D}_{\mathrm{AUSM}} = a_\beta \left[c_\Delta \mathbf{Q} + \Big(\mathbf{G}_0 \otimes \big(\mu_\Delta \nabla_{\mathbf{V}} M \big) \Big) \right] \mathbf{J} \; + \; s_p \, \mathbf{P}_p, \tag{A.45}$$

where the linearization coefficients are derived from the flux parameters as follows: $a_\beta = \rho_0 a_0$, $c_\Delta = -2K_u\phi$, and $s_p = -2K_p\phi/a_0$. The transformation matrix is $\mathbf{J} = \partial\mathbf{V}/\partial\mathbf{U}$, and the constituent matrices are defined as:

$$\mathbf{Q} = \mathrm{diag}(0, 1, 0), \qquad \mathbf{P}_p = \mathrm{diag}(1, u_0, H_0) \cdot [0, 0, 1], \qquad \mathbf{G}_0 = [1, u_0, H_0]^\top.$$

These matrices capture the velocity-diffusion ($\mathbf{Q}$) and pressure-diffusion ($\mathbf{P}_p$) couplings inherent to the scheme.

Because $\mathbf{D}_{\mathrm{AUSM}}$ generally does not share eigenvectors with $\mathbf{A}_0$, the characteristic modes are coupled. Using the MUSCL3 transport/diffusion symbols from Section A.1, the semi-discrete operator symbol is

$$\mathcal{L}(\theta) = \frac{\mathrm{i}}{2h} \left(\mathbf{A}_0 \, \Phi_A^{\mathrm{M3}}(\theta) - \mathbf{D}_{\mathrm{AUSM}} \, \Phi_D^{\mathrm{M3}}(\theta) \right), \qquad \theta \equiv kh, \tag{A.46}$$

and the complex frequencies are obtained from

$$\mathrm{i}\omega_n(\theta) = \mathrm{eig}_n\Big(\mathcal{L}(\theta) \Big). \tag{A.47}$$

For each eigenmode n, we define

$$v_{p,n}(\theta) = \frac{\Re(\omega_n)}{k}, \qquad v_{g,n}(\theta) = \frac{d\,\Re(\omega_n)}{dk}, \qquad \text{damping rate} = \Im(\omega_n). \tag{A.48}$$

A.3.3 Implementation: practical defaults and options

For the shaped AUSM+up scheme, we apply shaping and/or parameter adaptation only to the diffusive path.

ZPD bump (diffusive path). To achieve zero pass-band dissipation (ZPD), the diffusion shaper $g_D(\theta)$ is applied to $\widehat{\mathbf{F}}^{\mathrm{UP}}$. A typical setting is

$$r_{\mathrm{pass}} = 0, \qquad \theta_t = \theta_c, \qquad r_{\mathrm{high}} = 1, \qquad q \in \{4, 6\}. \tag{A.49}$$

Shock strengthening. To enhance robustness near strong discontinuities, the intrinsic dissipation parameters K_p and K_u are increased based on the shock sensor S:

$$K_p \leftarrow K_p^{(0)}(1-\omega)+K_p^{\mathrm{tgt}}\omega, \qquad K_u \leftarrow K_u^{(0)}(1-\omega)+K_u^{\mathrm{tgt}}\omega, \qquad \omega = \mathrm{clip}\Big(\frac{S-S_0}{1-S_0},\, 0,\, 1\Big). \tag{A.50}$$

Typical baseline values are $K_p^{(0)} \in [0.2, 0.35]$ and $K_u^{(0)} \in [0.7, 1.0]$.

References

1. C. K. Tam, Computational aeroacoustics: A wave number approach, no. 33, Cambridge University Press, 2012.

2. C. K. Tam, Computational aeroacoustics–issues and methods, AIAA journal 33 (10) (1995) 1788–1796.

3. C. K. Tam, J. C. Webb, Dispersion-relation-preserving finite difference schemes for computational acoustics, Journal of computational physics 107 (2) (1993) 262–281.

4. C. K. Tam, Z. Dong, Radiation and outflow boundary conditions for direct computation of acoustic and flow disturbances in a nonuniform mean flow, Journal of computational acoustics 4 (02) (1996) 175–201.

5. D. J. Bodony, S. K. Lele, Current status of jet noise predictions using large-eddy simulation, AIAA journal 46 (2) (2008) 364–380.

6. T. Colonius, S. K. Lele, Computational aeroacoustics: progress on nonlinear problems of sound generation, Progress in Aerospace sciences 40 (6) (2004) 345–416.

7. S. Moreau, The third golden age of aeroacoustics, Physics of Fluids 34 (3) (2022).

8. X. D. Li, M. Jiang, J. H. Gao, D. K. Lin, L. Liu, X. Y. Li, Recent advances of computational aeroacoustics, Applied Mathematics and Mechanics 36 (1) (2015) 131–140.

9. S. K. Lele, Compact finite difference schemes with spectral-like resolution, Journal of computational physics 103 (1) (1992) 16–42.

10. G. Ashcroft, X. Zhang, Optimized prefactored compact schemes, Journal of computational physics 190 (2) (2003) 459–477.

11. C. Bogey, C. Bailly, A family of low dispersive and low dissipative explicit schemes for flow and noise computations, Journal of Computational physics 194 (1) (2004) 194–214.

12. F. Q. Hu, M. Y. Hussaini, J. L. Manthey, Low-dissipation and low-dispersion Runge–Kutta schemes for computational acoustics, Journal of computational physics 124 (1) (1996) 177–191.

13. J. Berland, C. Bogey, O. Marsden, C. Bailly, High-order, low dispersive and low dissipative explicit schemes for multiple-scale and boundary problems, Journal of Computational Physics 224 (2) (2007) 637–662.

14. Y. Li, Y. X. Ren, A scale-aware dispersion-relation-preserving finite difference scheme for computational aeroacoustics, Physics of Fluids 35 (3) (2023).

15. C. Cheong, S. Lee, Grid-optimized dispersion-relation-preserving schemes on general geometries for computational aeroacoustics, Journal of Computational Physics 174 (1) (2001) 248–276.

16. S. C. Chang, The method of space-time conservation element and solution element—a new approach for solving the Navier-Stokes and Euler equations, Journal of computational Physics 119 (2) (1995) 295–324.

17. C. Williams, K. Duru, Full-spectrum dispersion relation preserving summation-by-parts operators, SIAM Journal on Numerical Analysis 62 (4) (2024) 1565–1588.

18. J. E. Hicken, Entropy-stable, high-order discretizations using continuous summation-by-parts operators, in: AIAA Aviation 2019 Forum, 2019, p. 3206.

19. A. E. Mattsson, W. J. Rider, Artificial viscosity: back to the basics, International Journal for Numerical Methods in Fluids 77 (7) (2015) 400–417.

20. K. Mattsson, M. Svärd, J. Nordström, Stable and accurate artificial dissipation, Journal of Scientific Computing 21 (1) (2004) 57–79.

21. M. Svärd, S. Mishra, Shock capturing artificial dissipation for high-order finite difference schemes, Journal of Scientific Computing 39 (3) (2009) 454–484.

22. M. Sun, K. Takayama, Conservative smoothing on an adaptive quadrilateral grid, Journal of Computational Physics 150 (1) (1999) 143–180.

23. S. K. Godunov, I. Bohachevsky, Finite difference method for numerical computation of discontinuous solutions of the equations of fluid dynamics, Matematičeskij sbornik 47 (3) (1959) 271–306.

24. A. Harten, High resolution schemes for hyperbolic conservation laws, Journal of computational physics 49 (3) (1983) 357–393.

25. C. W. Shu, S. Osher, Efficient implementation of essentially non-oscillatory shock-capturing schemes, Journal of computational physics 77 (2) (1988) 439–471.

26. G. S. Jiang, C. W. Shu, Efficient implementation of weighted ENO schemes, Journal of computational physics 126 (1) (1996) 202–228.

27. Z. J. Wang, R. F. Chen, Optimized weighted essentially nonoscillatory schemes for linear waves with discontinuity, Journal of Computational Physics 174 (1) (2001) 381–404.

28. E. Johnsen, J. Larsson, A. V. Bhagatwala, W. H. Cabot, P. Moin, B. J. Olson, S. K. Lele, Assessment of high-resolution methods for numerical simulations of compressible turbulence with shock waves, Journal of Computational Physics 229 (4) (2010) 1213–1237.

29. H. C. Yee, N. D. Sandham, M. J. Djomehri, Low-dissipative high-order shock-capturing methods using characteristic-based filters, Journal of computational physics 150 (1) (1999) 199–238.

30. H. C. Yee, B. Sjögreen, High order filter methods for wide range of compressible flow speeds, in: Spectral and High Order Methods for Partial Differential Equations: Selected papers from the ICOSAHOM'09 conference, June 22-26, Trondheim, Norway, Springer Berlin Heidelberg, 2010, pp. 327–337.

31. Z. Sheng, H. Zhang, Y. Wang, C. Xu, An improved high-order low dissipation weighted compact nonlinear scheme for compressible flow simulations, Physics of Fluids 36 (9) (2024).

32. J. Cai, W. Liu, High-order adaptive dissipation scheme based on vortex recognition for compressible turbulence flow, Commun. Comput. Phys. 35 (2024) 395–426.

33. Y. Li, C. Chen, Y. X. Ren, A class of high-order finite difference schemes with minimized dispersion and adaptive dissipation for solving compressible flows, Journal of Computational Physics 448 (2022) 110770.

34. S. Kawai, S. K. Lele, Localized artificial diffusivity scheme for discontinuity capturing on curvilinear meshes, Journal of Computational Physics 227 (22) (2008) 9498–9526.

35. S. Pirozzoli, Numerical methods for high-speed flows, Annual review of fluid mechanics 43 (1) (2011) 163–194.

36. C. Bogey, C. Bailly, D. Juvé, Noise investigation of a high subsonic, moderate reynolds number jet using a compressible large eddy simulation, Theoretical and Computational Fluid Dynamics 16 (4) (2003) 273–297.

37. W. G. Zeng, L. Liu, M. Q. Liu, L. J. Zeng, J. H. Pan, J. P. Yin, Y. X. Ren, High-order alternative finite difference scheme with minimized dispersion and adaptive dissipation for solving compressible flows, Physics of Fluids 37 (7) (2025).

38. H. C. Yee, B. Sjögreen, Numerical dissipation control in high-order methods for compressible turbulence: Recent development, Fluids 9 (6) (2024) 127.

39. R. J. LeVeque, Finite volume methods for hyperbolic problems, Vol. 31, Cambridge university press, 2002.

40. D. V. Nance, K. Viswanathan, L. N. Sankar, Low-dispersion finite volume scheme for aeroacoustic applications, AIAA journal 35 (2) (1997) 255–262.

41. B. Gutierrez Pimenta, A. V. B. Lopes, A. L. P. Maldonado, R. F. Bobenrieth Miserda, Optimized compact finite volume formulation with dispersion relation preserving characteristics in structured space discretizations, International Journal of Aeroacoustics 23 (5-6) (2024) 578–606.

42. P. L. Roe, Approximate riemann solvers, parameter vectors, and difference schemes, Journal of computational physics 43 (2) (1981) 357–372.

43. M. S. Liou, A sequel to AUSM, part II: AUSM+-up for all speeds, Journal of computational physics 214 (1) (2006) 137–170.

44. J. C. Strikwerda, Finite difference schemes and partial differential equations, 2nd Edition, Society for Industrial and Applied Mathematics, Philadelphia, PA, 2004.

45. E. B. Saff, R. S. Varga (Eds.), Padé and Rational Approximation, Academic Press, New York, 1977.

46. M. A. Luersen, R. Le Riche, Globalized Nelder–Mead method for engineering optimization, Computers & Structures 82 (23-26) (2004) 2251–2260.

47. E. M. Taylor, M. Wu, M. P. Martín, Optimization of nonlinear error for weighted essentially non-oscillatory methods in direct numerical simulations of compressible turbulence, Journal of Computational Physics 223 (1) (2007) 384–397.

48. E. Padway, H. Nishikawa, Resolving confusions over third-order accuracy of unstructured muscl, AIAA Journal 60 (3) (2022) 1415–1439.

Acknowledgements

First and foremost, I would like to express my deepest gratitude to my advisor, Professor Seongim Choi, for her invaluable guidance, patience, and support throughout my Master's studies. Her deep insight into Fluid Dynamics has been a constant source of inspiration, and her advice has been essential in shaping this research.

I would like to extend a special thanks to Professor Ray-Sing Lin. I am deeply grateful for his willingness to answer my countless questions and for the extensive help he provided whenever I faced difficulties. His detailed feedback and deep insights were instrumental in overcoming the challenges of this work.

I am also grateful to the members of the DDSDOL Laboratory for their helpful discussions, encouragement, and friendship.

I extend my sincere thanks to the committee members for their time and valuable comments on this thesis. Finally, I would like to dedicate this work to my family for their unconditional love and support, which has always been my greatest motivation.

Curriculum Vitae

Name	:	Chanho Park
Birth Date	:	March 13, 2000
Birth Place	:	Daegu, Republic of Korea
Permanent Address	:	123 Cheomdan-gwagiro, Buk-gu, Gwangju, Republic of Korea

Education

B.S. in Aeronautical and Mechanical Engineering, Korea Aerospace University (KAU)

M.S. in School of Mechanical Engineering, Gwangju Institute of Science and Technology (GIST)

Publications

International Journal

1. Chanho Park, Y. Kwak, Ray-Sing Lin, and Seongim Choi, "A Spectral Flux-Shaping Finite-Volume Method with Zero Pass-Band Dissipation: A Low-Dissipation Conservative Scheme Based on Upwind Flux Splitting," *Journal of Computational Physics (JCP)*, (Under Review).
2. Chanho Park, Y. Kwak, and Seongim Choi, "Physics-Constrained Inverse Acoustic Reconstruction via Projections Onto Convex Sets (POCS)," *Advances in Engineering Software (AIES)*, (Under Review).
3. Chanho Park, Woojin Lee, and Seongim Choi, "CFD analysis and design of bypass dual throat nozzle for high-performance fluidic thrust vectoring," *Advances in Engineering Software (AIES)*, Vol. 201, 103827, 2025. (Published).

International Conference

1. Chanho Park, Woojin Lee, and Seongim Choi, "Flow Analysis of Twin Supersonic Impinging Jets Using IDDES With Adaptive Mesh Refinement and Flow Prediction by Operator Learning Approach," *Asian Congress of Fluid Mechanics (ACFM)*, Seoul, Korea, Sep. 2025.
2. Chanho Park, Woojin Lee, and Seongim Choi, "Shape Design Optimization of Bypass Dual Throat Nozzle Using Reduced-Order Model with Machine Learning," *Asia-Pacific International Symposium on Aerospace Technology (APISAT)*, Adelaide, Australia, Oct. 2024.
3. Chanho Park and Seongim Choi, "A Numerical Study on Nozzle Thrust Vectoring and Ground Effects for V/STOL Aircraft," *International Congress of Theoretical and Applied Mechanics (ICTAM)*, Daegu, Korea, Aug. 2024.